EES Batteries

PERSPECTIVE

View Article Online
View Journal

Cite this: DOI: 10.1039/d6eb00054a

Advancing cryogenic electron microscopy towards the mechanistic understanding of metal electrodes and interphases

Yaolin Xu, [a,c] Kang Dong, [b] Zdravko Kochovski, [a] Qingping Wu *[a,f] and Yan Lu *[a,d,e]

Received 9th March 2026,
Accepted 12th March 2026

DOI: 10.1039/d6eb00054a

rsc.li/EESBatteries

Since its introduction to battery research in 2017, cryogenic electron microscopy (cryo-EM) has emerged as a powerful tool for probing the delicate structures of Li metal electrodes and their interphases. It has recently expanded to post-Li (*e.g.*, Na, K, Zn, Mg, Ca, and alloy) metal batteries and anode-free systems, offering new opportunities to understand complex interfacial phenomena. Despite these advances, significant challenges persist in fully leveraging cryo-EM across diverse battery chemistries and architectures. This perspective highlights the capabilities and inherent limitations of cryo-EM for elucidating the mechanisms of Li and post-Li metal deposition, as well as metal–electrolyte interphases in batteries with both liquid and solid electrolytes. Additionally, we present the most recent progress and key challenges in the application of cryo-EM to metal battery research. We also propose perspectives for further advancement, including standardizing workflows, upgrading instrumentation, developing new methodologies, and integrating cryo-EM with complementary characterization techniques to fully harness its potential in the development of next-generation metal batteries.

Broader context

The development of high-energy-density and safe rechargeable batteries is essential to achieving global decarbonization and electrification targets. Metal-based batteries, including lithium and emerging post-lithium systems, offer significant advantages due to their high theoretical capacities and elemental abundance. However, the unstable electrode–electrolyte interphases formed at metal anodes remain a critical barrier to practical implementation. These interfaces are chemically complex, highly reactive, and extremely sensitive to conventional characterization techniques. Cryogenic electron microscopy (cryo-EM) has recently emerged as one of the most powerful and reliable tools for directly visualizing these fragile structures at atomic resolution. This perspective provides a timely and comprehensive overview of how cryo-EM has advanced the mechanistic understanding of metal anodes and their interphases across a range of battery chemistries. In addition to highlighting key discoveries, this article outlines current challenges and offers forward-looking strategies for expanding the capabilities of cryo-EM. These insights are crucial for guiding rational interface design and accelerating the development of next-generation metal batteries for sustainable energy storage.

1. Introduction

Lithium (Li)-ion batteries dominate the current battery market; however, unfortunately, they cannot meet the increasing demand for energy density and sustainability for future use.[1] In the search for more energy-dense and sustainable energy storage solutions, Li metal batteries (LMBs)[2–5] and their post-Li counterparts, such as sodium (Na),[6] potassium (K),[7] zinc (Zn),[8] calcium (Ca),[9] magnesium (Mg),[10] alloy metals,[11] and anode-free batteries,[12] have garnered significant attention. However, these batteries face challenges stemming from unstable metal electrodes and electrode–electrolyte interfaces. In particular, stable cycling of reactive metal anodes is hindered by issues such as non-uniform or dendritic metal deposition and unstable solid–electrolyte interphase (SEI) for-

[a]*Institute of Electrochemical Energy Storage, Helmholtz-Zentrum Berlin für Materialien und Energie, Hahn-Meitner-Platz 1, 14109 Berlin, Germany. E-mail: yan.lu@helmholtz-berlin.de, qingping.wu@helmholtz-berlin.de*
[b]*Multi-disciplinary Research Division, Institute of High Energy Physics Chinese Academy of Sciences, 100049 Beijing, China*
[c]*Department of Applied Physics, Aalto University, 02150 Espoo, Finland*
[d]*Helmholtz Institute for Polymers in Energy Applications Jena (HIPOLE Jena), Lessingstrasse 12-14, 07743 Jena, Germany*
[e]*Institute for Technical and Environmental Chemistry, Friedrich-Schiller-Universität Jena, Fürstengraben 1, 07743 Jena, Germany*
[f]*Chongqing Institute of Green and Intelligent Technology, Chinese Academy of Sciences, 400714 Chongqing, China*

mation from parasitic reactions between the reactive metals and the electrolytes.[13,14] These problems lead to rapid capacity decay and serious safety risks, including electrical short-circuiting.

Future developments of Li and post-Li metal batteries require a mechanistic understanding of key electrochemical processes, including metal deposition and dissolution, formation and evolution of a SEI, and the interplay between these processes. Such insights are essential to guide the rational design of electrodes and batteries. Visualizing metal electrodes and their interfaces as well as their dynamic evolution at the nano- and atomic scale, for instance, using scanning and transmission electron microscopy (S/TEM), is crucial for this purpose.[15,16] However, the high reactivity of these metals and the low atomic number of light elements like Li render them highly susceptible to electron beam damage, posing significant challenges for imaging reactive metal deposits and SEIs in their native states, particularly at high spatial resolution.

Cryogenic electron microscopy (cryo-EM) has been successful in resolving the atomic structures of biological macromolecules,[17] the nanostructures of soft matter materials,[18] and other sensitive materials.[19] Cryo-EM preserves highly reactive and beam-sensitive materials by rapidly vitrifying the specimen and maintaining it at cryogenic temperatures during transfer and imaging. Rapid plunge-freezing immobilizes structural and chemical configurations in a near-native state, suppressing solvent rearrangement and preventing morphological artifacts associated with drying or air exposure. Under cryogenic conditions, electron beam-induced damage and radiolysis are substantially mitigated, enabling low-dose imaging and even atomic-resolution characterization of sensitive battery materials such as lithium metal anodes and SEIs.[19,20] This achievement, recognized with the 2017 Nobel Prize in Chemistry, highlights its transformative impact. Cryo-EM was first introduced to study the atomic structure of Li deposits in 2017.[20] It has attracted substantial research interest in materials science, particularly for sensitive materials such as battery materials,[21–28] hybrid perovskite solar cells,[29,30] and metal–organic frameworks (MOFs)/covalent organic frameworks (COFs).[31,32] The cryogenic operating conditions of cryo-EM (*e.g.*, liquid-nitrogen cooling and transfer; sample temperatures typically 80–100 K (−193 to −173 °C)) reduce beam-induced damage and preserve near-native states, enabling 2D and 3D analyses of structure and chemistry at sub-nanometer and, in favorable cases, atomic resolution. As for conventional electron microscopy (EM), cryo-EM encompasses a suite of microscopic and spectroscopic methods. These include cryogenic focused ion beam-scanning electron microscopy (cryo-FIB-SEM) and tomography, cryogenic transmission electron microscopy (cryo-TEM) with selected-area electron diffraction (SAED) and electron tomography (cryo-ET), and cryogenic scanning transmission electron microscopy (cryo-STEM) with associated X-ray energy-dispersive spectroscopy (EDX) and electron energy-loss spectroscopy (EELS) for spectrum imaging and mapping (Scheme 1). Cryo-TEM/STEM provides real-space morphology and Z-contrast, while EDX/EELS delivers elemental and electronic-structure information. In combination, elemental mapping and tomography reveal 2D and 3D chemical distributions and reconstruct the 3D structure of beam- and air-sensitive samples such as battery materials.

Cryo-EM is particularly effective for studying highly reactive and electron-sensitive metal deposits (*e.g.*, Li, Na, K, Zn, Ca, Mg, and alloys), along with their interphases, providing

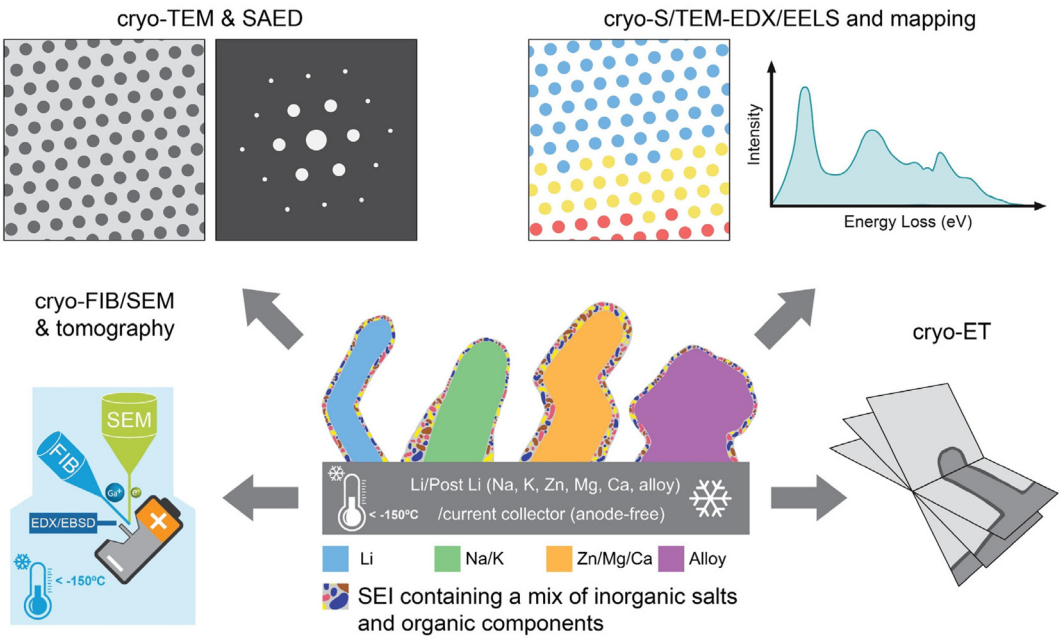

Scheme 1 Overview of cryo-EM techniques for characterizing sensitive metal electrodes and interphases: from Li to post-Li.

insights into their nanostructure, chemical composition, and crystallographic properties. To date, most cryo-EM studies reported in the literature have focused on Li deposits and the SEI layer in LMBs. More recently, cryo-EM has gained increasing attention for the study of solid-state lithium metal batteries (SSLMBs) and post-Li metal batteries, particularly those based on sodium.[33] While several recent reviews have summarized cryo-EM workflows and general applications in battery research, a systematic analysis centered specifically on metal electrodes and their interphases across different electrolyte environments remains limited. In particular, a unified perspective that connects structural observations from cryo-EM with mechanistic implications for metal deposition, dendrite evolution, and interfacial instability in both Li and post-Li systems is still lacking. Addressing this gap is critical for advancing the rational design of stable metal anodes in next-generation batteries. Although cryo-EM has also been widely used to study non-metal battery materials, this Perspective specifically focuses on Li and post-Li metal anodes and their interphases, where cryo-EM provides unique capabilities for probing highly reactive metal interfaces and metal deposition behaviors.

This Perspective provides a mechanistic understanding of the structure and dynamics of both Li and post-Li metal electrodes as well as their interphases, as revealed through cryo-EM. Additionally, it outlines strategic directions for future development, aiming to achieve stable and energy-dense metal batteries. While several previous reviews or perspectives have discussed cryo-EM characterization of sensitive battery materials,[23,25–28] currently there is no focused work dedicated specifically to cryo-EM studies of metal electrodes and interphases in rechargeable batteries. This is particularly relevant for the rapidly growing body of work on SSLMBs and post-Li metal batteries for next-generation energy storage. Our work seeks to fill that gap by providing a timely overview of recent achievements in cryo-EM research on Li and post-Li metal batteries while also guiding the advancement of cryo-EM methodologies for studying sensitive electrochemical materials and interphases, with broader implications in the field of materials science.

2. Cryo-EM for mechanistic studies of Li metal anodes and SEIs

2.1 Li metal anodes and SEIs in liquid electrolytes

LMBs, including Li–sulfur,[34] Li–air,[35] and SSLMBs,[36] are highly attractive for significantly enhancing the energy density of batteries. This appeal arises from the unique and exceptional properties of Li metal anodes, which include an ultrahigh theoretical capacity (3860 mAh g^{-1}, approximately 10 times that of graphite anodes), the lowest electrochemical potential (−3.4 V *vs.* standard hydrogen electrode), and a low density (0.534 g cm^{-3}).[37] Despite these advantages, the commercialization of LMBs has been severely hindered by challenges such as dendritic Li deposits and unstable SEIs.[38] Achieving a comprehensive understanding of Li nucleation and growth, as well as the nanostructure and chemistry of SEIs, is essential for the rational design and development of advanced Li metal anodes and ultimately achieving stable and high-performance operation of LMBs. Since its introduction to the study of sensitive battery materials, cryo-EM has primarily been used to investigate Li deposition and SEI formation in organic liquid electrolytes. More recently, its application has expanded to the investigation of SSLMBs. This section summarizes recent advances in the characterization of Li deposits and associated SEIs achieved through cryo-EM.

2.1.1 Morphology and structural evolution of Li deposits. Metallic Li^0 deposition occurs as a result of the electrochemical reduction of Li^+. The resultant Li deposits are prone to nonuniformity or even dendritic growth. This behavior can, on one hand, lead to the formation of inactive ("dead") Li during repetitive plating and stripping, resulting in low coulombic efficiency (CE).[39] On the other hand, dendritic Li can penetrate polymer separators, potentially causing internal short circuits and significant safety concerns. Addressing these challenges fundamentally requires a deep understanding of Li plating processes, including nucleation, growth and evolution.

The Li nucleation process (*e.g.*, formation of Li^0 crystal nuclei) remains mysterious and elusive.[13] Nevertheless, thanks to cryo-EM's unique ability of resolving beam-sensitive samples from the atom scale to the nanoscale, some progress has been achieved in unveiling the initial stage of Li deposition. For example, Wang *et al.*[40] investigated the nanostructure of Li deposits at various states during the nucleation and growth processes with cryo-EM and identified a disorder-to-order transition in Li deposits as a function of deposition current density and time. This glass-to-crystalline transition was also observed in other metals, including Na, K, Mg and Zn during the very early stage of nucleation. As the deposition time increased, the crystalline domains grew from approximately 5 nm to over 50 nm. A similar crystallographic transition was observed by Dong *et al.*[41] during the growth of Li deposits, progressing from Li balls to Li dendrites. Using a carbonate-based electrolyte at deposition capacities ranging from 0.05 to 1.0 mAh cm^{-2}, the coexistence of two distinct Li deposition morphologies, Li balls and Li dendrites, has been revealed. Cryo-TEM analysis showed that the ball-like deposits were predominantly amorphous with some crystalline domains, while the dendritic whiskers exhibited a single-crystalline structure. In another study that integrated atomic force microscopy and environmental transmission electron microscopy (AFM-ETEM), Li balls were identified as the initial nuclei or early deposition morphologies, evolving into whisker-like Li dendrites under conditions that exceed the diffusion-limiting current.[42]

The growth process of Li deposits has been revealed by investigating the morphology and crystallography of Li deposits with cryo-EM. Under normal working conditions, Li deposition and SEI growth are intertwined, and the morphology of Li deposition is thereby influenced by the SEI layer. Li *et al.*[20]

investigated the crystallographic growth behavior of Li dendrites using cryo-TEM-based SAED. Their findings revealed that Li dendrites grow along the ⟨111⟩, ⟨110⟩, or ⟨211⟩ directions in carbonate-based electrolytes, with a preference for the ⟨111⟩ direction (Fig. 1a). Kinks were observed during dendrite growth, where changes in the growth direction could occur. Cryogenic high-resolution transmission electron microscopy (cryo-HRTEM) further elucidated the atomic structure of the Li

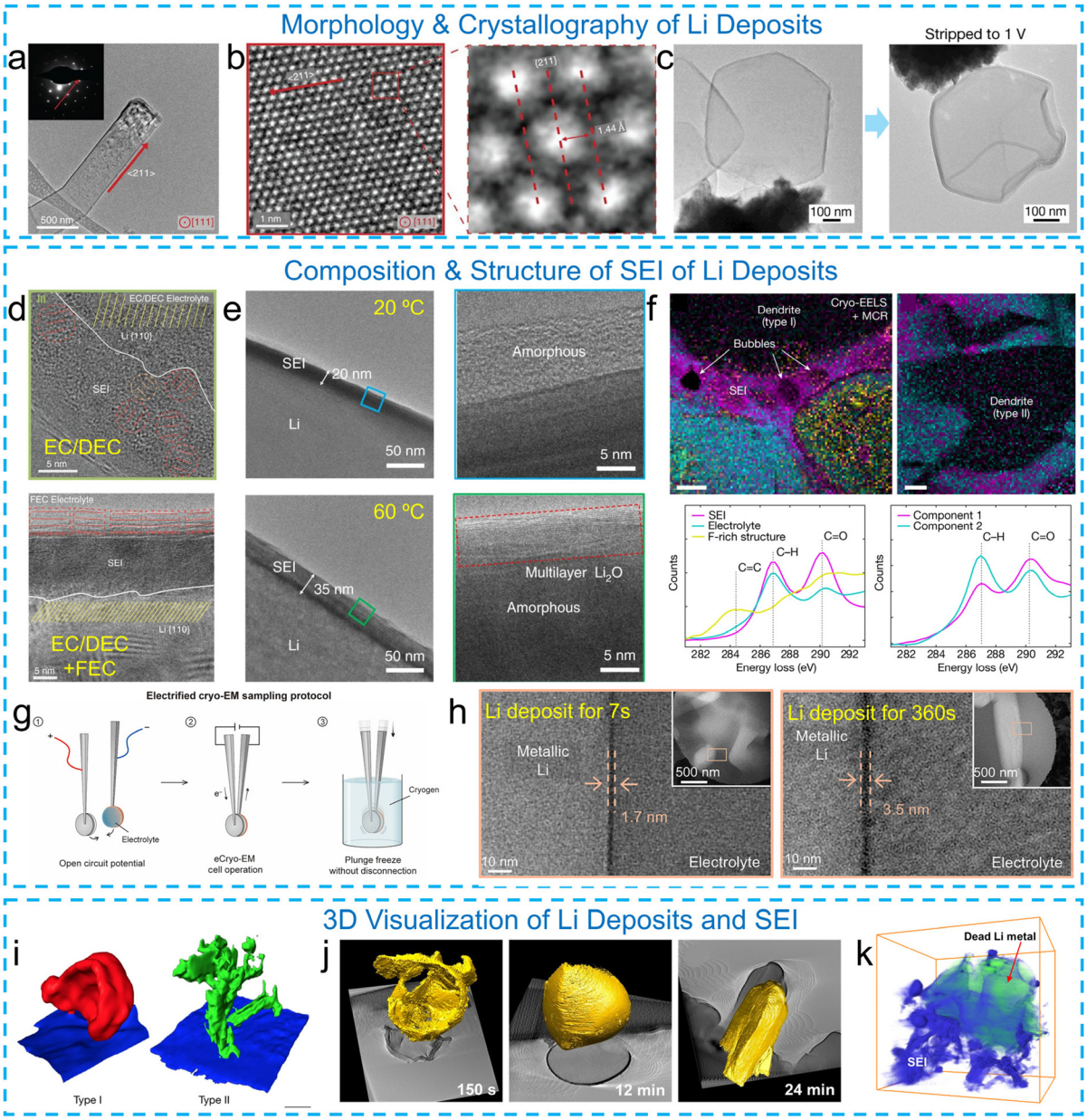

Fig. 1 Cryo-EM characterization of Li deposits and SEIs. (a) Cryo-TEM images and SAED patterns of Li deposits along the ⟨111⟩ direction. (b) Cryo-HRTEM images showing the atomic structure of Li deposits. (c) Cryo-EM images of faceted Li particles on a Cu substrate showing poor interfacial contact after deposition (left) and a partially stripped Li particle after electrochemical stripping to 1 V. Reproduced with permission from ref. 43. Copyright 2023 Springer Nature. (d) SEI layers formed in electrolytes with and without an FEC additive, respectively. Reproduced with permission from ref. 20. Copyright 2017 The American Association for the Advancement of Science. (e) SEI layers formed at 20 and 60 °C, respectively. Reproduced with permission from ref. 46. Copyright 2019 Springer Nature. (f) The contents of SEIs grown on two types of Li dendrites revealed by cryo-STEM-EELS and mapping. Reproduced with permission from ref. 48. Copyright 2018 Springer Nature. (g) eCryo-EM sampling protocol, and (h) corresponding images of Li deposits evolving with deposition time in 4 M lithium bis(fluorosulfonyl)imide (LiFSI) in 1,2-dimethoxyethane (DME). Reproduced with permission from ref. 50. Copyright 2025 The American Association for the Advancement of Science. (i) 3D reconstructions of the dendrite structures from cryo-FIB/SEM. Reproduced with permission from ref. 48. Copyright 2018 Springer Nature. (j) 3D cryo-ET showing the morphological evolution of Li deposits. Reproduced with permission from ref. 49. Copyright 2022 Elsevier. (k) 3D visualization of the SEI husk and "dead" Li after stripping revealed by cryo-STEM tomography. Reproduced with permission from ref. 52. Copyright 2021 Elsevier.

dendrites (Fig. 1b). Additionally, diffraction-like patterns of Li dendrites can be calculated by processing cryo-HRTEM images using algorithms such as fast Fourier transform (FFT), providing insights into the periodicity and orientation of the dendritic structure. In contrast, at an ultrafast deposition rate that outpaces SEI formation, Li deposition is decoupled from SEI growth. Under such conditions, Yuan *et al.* demonstrated using cryo-TEM that the intrinsic morphology of Li deposition is a rhombic dodecahedron, independent of the electrolyte composition or current collector.[43] Furthermore, cryo-TEM provides direct evidence that this intrinsic morphology leads to a distinct failure mechanism under practical cycling conditions. Cryo-TEM imaging (Fig. 1c) reveals that the rhombic dodecahedra make only point-like contact with the Cu current collector, resulting in poor electronic connectivity. During stripping, this limited contact prevents complete oxidation of the deposited Li, leaving behind substantial metallic residues. Cryo-TEM images of partially stripped particles show a shrunken rhombic dodecahedron core encapsulated within the SEI, confirming that electrical disconnection is the dominant origin of inactive Li formation at ultrafast deposition rates. This contrasts sharply with low-current deposition (1 mA cm^{-2}), where columnar Li maintains intimate substrate contact and stripping leaves mostly hollow SEI shells with minimal inactive Li. These observations establish cryo-TEM as a powerful tool for distinguishing SEI-derived failure from electronically isolated metallic Li and highlight that ultrafast-grown faceted Li suffers from an electrical-contact-limited failure mode despite its uniform morphology.

2.1.2 Chemical composition and formation mechanism of SEIs. SEIs, first introduced by Peled in 1979,[44] are passivation layers, typically 5 to 100 nm thick, that form on the electrode surface as a result of electrolyte decomposition and the reactions with electrode materials. Understanding the chemical composition and spatial distribution within the nanoscale thickness of SEIs is essential, as it regulates the kinetics of ion diffusion and charge transfer at the interface of (electro)chemical reactions, thereby determining key battery performance metrics, including capacity, operational stability, and safety. Despite decades of research, SEIs are still regarded as "the most important but least understood components" due to their complexity in chemistry and structure.[45] Nanoscale investigations of SEIs, such as those using TEM, are particularly challenging because of the electron beam sensitivity of lithium salts and organic compounds within the interphase. Cryo-EM facilitates the characterization of the SEI by preserving its native state at cryogenic temperatures and significantly suppressing electron beam damage. In recent years, this technique has provided critical insights into the structure and chemistry of the SEIs formed in various electrolytes.

The nanostructure and chemistry of SEIs depend on the electrolyte types (carbonate- or ether-based liquid electrolytes and solid electrolytes) and operating conditions (*i.e.*, current, temperature, and stack pressure). Using cryo-TEM, Li *et al.*[20] validated two SEI nanostructures, mosaic and multilayered, originally proposed by Peled and Aurbach and their co-workers in 1979 and 1994, respectively. Specifically, in ethylene carbonate (EC) and diethyl carbonate (DEC) electrolytes, the SEI structure adopts a mosaic structure, comprising nanocrystalline inorganic salt domains (Li_2O, Li_2CO_3, LiF, *etc.*) embedded within an organic matrix of Li alkyl carbonates. When fluoroethylene carbonate (FEC) is used as an additive, the SEI layer on Li forms a multilayer structure, with an organic layer sandwiched between the Li metal and inorganic salt layer (Fig. 1d). The formation of the SEI is also influenced by the operation temperature. Cryo-EM revealed that at an elevated temperature of 60 °C, a thicker (~35 nm) and multilayered SEI formed, compared to an amorphous SEI with a thickness of ~20 nm at 20 °C (Fig. 1e).[46] The outer interface layer, composed of Li_2O grains, is attributed to enhanced kinetics at higher temperatures and is mechanically more robust than the inner polymeric layer, leading to stable cycling with a coulombic efficiency of 99.3%. Cryo-EM-based SAED, EDX and EELS can be utilized to obtain detailed insights into the chemistry and structure of the SEI. Shadike *et al.*[47] employed cryo-STEM-based EELS to identify lithium hydride (LiH) in the SEI for the first time, and this finding was corroborated through synchrotron-based X-ray diffraction. Similarly, Zachman *et al.*[48] demonstrated and quantified the compositional differences in SEI layers formed on two distinct types of Li deposits using cryo-STEM-based EELS and elemental mapping (Fig. 1f).

The SEI layer is found to evolve in thickness, morphology, and chemistry as the underneath Li deposits grow. This process imposes stress on the SEI layer, potentially causing it to crack and exposing fresh Li to the electrolyte.[49] To overcome the limitations of conventional cryo-EM in capturing transient interfacial states, Wang *et al.*[50] developed an electrified cryo-EM (eCryo-EM) technique (Fig. 1g) that enables direct imaging of SEI formation dynamics (Fig. 1h). Using this method, they revealed two distinct growth regimes, which are initially reaction-limited and then diffusion-limited, that have similar ion transport properties but significantly different reactivity. Their findings indicate that electrolyte reactivity, rather than transport through the SEI, is the dominant factor governing coulombic efficiency (CE).

2.1.3 3D visualization of Li deposits and interphases. Combined with cryo-FIB and cryo-ET, cryo-S/TEM has been employed to investigate the three-dimensional (3D) structure and chemistry of Li deposits and SEIs. Cryogenic temperatures protect Li deposits and interfaces from gallium ion beam damage during FIB cutting and minimize electron beam damage, enabling 3D tomographic analysis with accumulated electron beam exposure over a series of images acquired for ET. Zachman *et al.*[48] highlighted the 3D morphological differences between two types of Li dendrites using cryo-FIB tomography (Fig. 1i). Using cryo-FIB tomography combined with EDX, Lee *et al.*[51] demonstrated 3D reconstructions of porous electrochemical Li deposits and the interfaces formed in various liquid electrolytes. They also quantified the pore volumes within the deposited Li bulk. Meanwhile, Jie *et al.*[49] utilized cryo-ET to reveal the sphere-to-column morphological evolution and growth of Li deposits under an *operando* poly-

merized SEI layer (Fig. 1j). Han *et al.*[52] employed cryo-ET combined with EELS to achieve 3D visualization of both the SEI husk and the "dead" Li following Li stripping (Fig. 1k). This 3D reconstruction further revealed that the SEI does not collapse upon delithiation but instead buckles into a hollow, wrinkled framework, within which electronically isolated metallic Li becomes trapped. The cryo-ET tilt series and cross-sectional slices show that these dead Li particles sit on top of the empty SEI husks with no conductive pathway to the current collector, indicating that mechanical deformation of the SEI and non-uniform stripping jointly induce electronic disconnection-driven inactive Li formation. Such SEI-mediated isolation, rather than dendritic fracture, emerges as a dominant failure mechanism even after a single cycle.

2.2 Li metal anodes and interfaces with solid electrolytes

Solid-state batteries (SSBs) with Li metal anodes offer significantly improved energy density compared to liquid electrolyte-based Li batteries and have the potential to fundamentally address the safety issues associated with Li anodes. However, the high electro-/chemical reactivity of Li metal leads to parasitic reactions with solid electrolytes (SEs), resulting in the formation of an interfacial layer with a complex chemical composition. The physical properties of this nanoscale interfacial layer, such as thickness, morphology, mechanical stability, and ion and electron conductivity, profoundly influence the macroscopic electrochemical performance of batteries. Understanding the chemistry and structure of this interphase is therefore of critical importance. Leveraging advances in the research on liquid electrolyte-based LMBs, cryo-EM has been employed to investigate the interfaces between Li and SEs, including inorganic solid electrolytes (ISEs),[51,53,54] solid polymer electrolytes (SPEs),[55–59] and semi-solid (or quasi-solid) electrolytes (semi-SEs).[60]

2.2.1 Li metal interfaces with inorganic solid electrolytes: dense contacts. As high stacking pressures are applied during the operation of SSBs, especially when ISEs are used, Li deposits and SEI layers are typically embedded within SEs, rendering them inaccessible for most characterization probes. Therefore, this often necessitates the use of supplementary cryo-FIB techniques to expose buried interfaces for detailed cryo-EM investigations.[61] Lee *et al.*[51] employed cryo-FIB/SEM combined with EDX to reveal the structures of Li deposits formed at the interfaces in thin-film Li|LiPON|LCO SSBs, where LiPON refers to an ISE (lithium phosphorus oxynitride) and LCO refers to a $LiCoO_2$ cathode (Fig. 2a). Sun *et al.*[53] demonstrated Li nucleation and propagation within Li_3PS_4 (LPS)-based ISEs using cryo-TEM (Fig. 2b). Cheng *et al.*[54] investigated the interphase formed between Li and LiPON using a cryogenic lift-out method that combined cryo-FIB and cryo-S/TEM. They identified a multilayer SEI interphase of approximately 76 nm thick, consisting of several inorganic Li salts, such as Li_2O, Li_3N, and Li_3PO_4, embedded in an amorphous matrix, with concentration gradients of nitrogen (N) and phosphorus (P) revealed by EELS (Fig. 2c). This SEI forms a multilayer mosaic structure composed of nanocrystals embedded in a dense amorphous matrix, providing an electronically insulating yet ionically conductive passivation layer that prevents continuous LiPON decomposition and ensures long-term interfacial stability with Li metal.

2.2.2 Li metal interfaces with polymer-based solid electrolytes: conformal coupling. SPEs offer soft, flexible interfaces with Li metal, enabling better interfacial contact and ionic conduction compared to their inorganic counterparts. However, their low mechanical strength and complex SEI formation present distinct challenges for interfacial characterization, where cryo-EM proves particularly effective in resolving nanoscale features and chemical distributions. Lin *et al.*[55] examined the 3D morphologies of Li deposits with cryo-ET and SEI distributions using cryo-STEM combined with EDX mapping. These deposits are formed in succinonitrile (SN)-based SPEs with or without FEC additives (Fig. 2d). Notably, the Li deposits formed in an SN-SPE exhibited a filament-shaped morphology without a passivating SEI layer, attributed to stress–corrosion–cracking behavior and sustained parasitic reactions between freshly deposited Li and the polyacrylic backbones and succinonitrile plasticizer in the SPE. In contrast, the Li deposits formed in an FEC-SPE showed a dome-shaped morphology with a thin and conformal SEI layer containing randomly oriented crystalline Li_2O grains and amorphous LiF. This behavior reflects a fundamental SEI failure mechanism in SN-based SPEs, where the decomposition products permeate the entire Li filament instead of forming a surface-confined, electronically insulating SEI, leading to unpassivated corrosion and chemomechanical cracking. The FEC-SPE enables the formation of a thin, dense, and LiF-rich mosaic SEI that is electronically insulating yet ionically conductive, effectively suppressing parasitic reactions and preventing chemomechanical cracking, thereby stabilizing the Li–SPE interface.

2.2.3 Li metal interfaces with semi-solid electrolytes: hybrid interphases with mixed phases. In addition to ISEs and SPEs, semi-SEs have emerged as a promising class of materials that combine the mechanical stability of solids with the ionic conductivity and interfacial wettability of liquids. These systems are often composed of polymer matrices swollen with liquid components, which offer improved interfacial contact with lithium metal and the potential to suppress dendrite growth. However, the hybrid nature of semi-solid electrolytes complicates the formation and evolution of SEIs, which are influenced by both solvent chemistry and polymer structure. Understanding the composition, structure, and spatial distribution of SEIs in such environments requires high-resolution, low-damage characterization techniques. In this context, cryo-EM has proven to be a powerful tool to probe SEI formation in quasi-solid systems under native-like conditions. Zhao *et al.*[62] investigated a semi-solid electrolyte system based on polyamide (PA, nylon) and employed cryo-TEM to elucidate the resulting SEI on Li metal (Fig. 2e). The cryo-TEM images revealed a distinct SEI shell layer, ~23 nm thick, composed of a mosaic-like mixture of amorphous domains and scattered inorganic nanocrystals. FFT analysis identified Li_2CO_3, LiF, and Li_2O as the major crystalline components. Further analysis confirmed the incorporation of Li_3N, which appeared as a

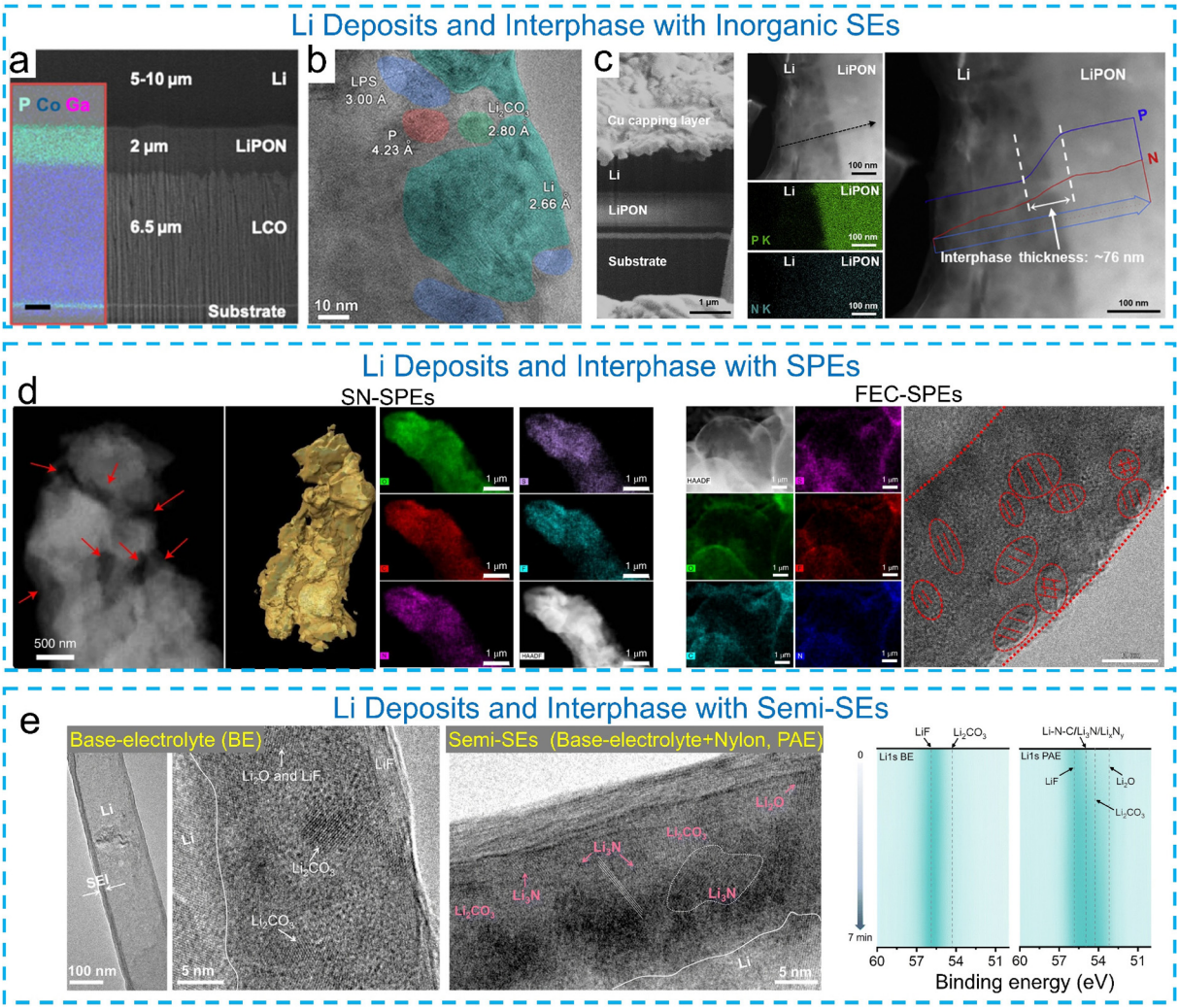

Fig. 2 (a) Cryo-FIB/SEM imaging and EDX mapping showing the Li|LiPON|LCO interfaces. Reproduced with permission from ref. 51. Copyright 2019 American Chemical Society. (b) Li deposits formed inside Li_3PS_4-based ISEs evidenced by cryo-TEM. Reproduced with permission from ref. 53. Copyright 2021 American Chemical Society. (c) Cryo-FIB-SEM cross-sectional image of the Li/LiPON sample and Cryo-STEM images of the Li/LiPON interface, the corresponding EDX line scan of P and N signals along the Li–LiPON interface and the interphase composition. Reproduced with permission from ref. 54. Copyright 2020 Elsevier. (d) Morphology of Li deposits and interphases formed in an SN (plasticizer succinonitrile)-SPE and an FEC (additive fluoroethylene carbonate)-SPE, respectively. Reproduced with permission from ref. 55. Copyright 2022 Springer Nature. (e) Cryo-TEM images of Li deposits in a base electrolyte (1 M LiPF6 in EC : DEC (1 : 1 by vol%) + 5 wt% FEC, namely, BE) and semi-SEs (Nylon in a base electrolyte, namely, PAE), and the corresponding 2D Li 1s contour HR-XPS data of the SEI. Reproduced with permission from ref. 62. Copyright 2025 The Royal Society of Chemistry.

dense and continuous phase throughout the SEI. This nitrogen-derived interphase is attributed to the decomposition of amide-rich PA and is known to enhance SEI stability, ionic conductivity, and Li deposition uniformity.

Compared with the SEI formed in LMBs with liquid electrolytes, the chemistry and structure of interphase layers in batteries with ISEs, SPEs and semi-SEs are less understood. This is partially attributed to the fact that the buried interphase layer in SSBs is more difficult to expose and probe in an "intact" state prior to cryo-EM characterization. In addition, interfacial chemistry associated with ISEs tends to consist of inorganic Li salts, while organic compounds could exist in the SEI layer formed in SPE-based batteries. Across liquid, solid, and polymer electrolytes, SEI failure and dendrite growth arise from electrolyte-dependent breakdown pathways: liquid electrolytes suffer from porous, unstable SEIs that fracture and expose fresh Li, solid electrolytes experience electronic leakage or mechanical mismatch that drives filament penetration, and polymer electrolytes often fail to form a dense passivating SEI at all, leading to sustained parasitic reactions, stress-corrosion cracking, and uncontrolled filamentary Li growth. These structural insights also suggest that electrolyte formulation and interphase chemistry can be tuned to regulate Li nucleation behavior and stabilize preferred growth modes, thereby suppressing dendritic deposition and promoting more uniform Li metal growth.

3. Cryo-EM as an emerging tool for investigating post-lithium metal anodes and interphases

In recent years, post-Li metal batteries based on Na, K, Zn, Ca, Mg, and various alloy anodes have received growing attention as promising alternatives to LMBs, as well as anode-free systems, largely due to their greater natural abundance and lower cost.[63,64] Despite their potential, the fundamental understanding of the electrode–electrolyte interfaces in these systems remains limited. Similar to Li metal, post-Li metals are highly reactive and prone to side reactions, and their interfaces are often unstable and structurally heterogeneous. Moreover, their sensitivity to ambient conditions and electron beam damage presents substantial challenges for characterization using conventional techniques.

Cryo-EM, which has proven highly effective in revealing the nanostructure and chemical evolution of Li metal interphases, is increasingly being applied to post-Li metal systems. This technique enables the preservation and visualization of delicate interfacial structures under near-native conditions, offering new opportunities to unravel the mechanisms of metal deposition, SEI formation, and interphase degradation. Current cryo-EM studies have primarily focused on Na, owing to its electrochemical similarity to Li. In contrast, research on K, multivalent metals such as Ca and Mg, and alloy-based and anode-free systems is still in its early stages. The following sections review recent advances in cryo-EM investigations of these emerging systems, with emphasis on the structural and chemical characteristics of their interphases and the mechanistic insights they provide for interface engineering.

3.1 Structural and chemical insights into Na metal anodes and interphases

In the research field of Na metal batteries, cryo-EM was first employed to study Na metal anodes in 2021, attracting considerable research attention. This technique has since been utilized to investigate the nucleation and growth of Na deposits and their interphases in various electrolytes and working conditions.[65–71] For instance, Zhu *et al.*[65] used cryo-TEM to capture Na nucleation in a concentrated phosphate-based electrolyte (Fig. 3a). The initially formed Na nuclei were in the size range of 4–10 nm, surrounding a Na "embryo" of approximately 30 nm, and were embedded within an amorphous matrix. An amorphous SEI layer of 6–10 nm thickness was also identified. Cryo-TEM provides critical insights into the microstructure of Na deposition under varying conditions. Similar to Li, electrolyte modification significantly influences Na deposition behavior. For example, dendritic Na deposition was observed in a $NaPF_6$-diglyme electrolyte, whereas uniform Na deposits were formed in this electrolyte but contained the cetyltrimethylammonium bromide (CTAB) additive (Fig. 3b).[66]

The Na deposition morphology is closely tied to the electrolyte formulation. In carbonate-based electrolytes, such as NaPF6 in EC/DMC, Na dendrites exhibit typical growth, while dendrites formed in FEC-containing electrolytes ($NaPF_6$-EC/DMC/FEC) display a higher length-to-diameter (l/d) aspect ratio. Furthermore, the morphology of Na dendrites and their SEI layers evolved during cycling, often accompanied by SEI thickening (Fig. 3c).[67] They also showed that a thin (~30 nm) and layered SEI, consisting of a NaF-rich amorphous outer layer and a Na_3PO_4-like inner layer, is formed in an FEC-containing carbonate electrolyte and remains stable over cycling, exhibiting a similar composition and structure after 10 cycles. In contrast, the SEI formed in an FEC-free electrolyte is significantly thicker (up to several hundred nanometers) and unstable over cycling. This SEI comprises single-crystalline Na_3PO_4 rods and Na_2CO_3 intermixed with "dead" Na after 10 cycles. In another study, Zheng *et al.*[68] showed that the SEI formed in both $NaPF_6$-PC-FEC and $NaPF_6$-PC electrolytes exhibits a mosaic structure composed of both organic and inorganic components. The SEI formed in the FEC-containing electrolyte is thinner (~40 nm) and enriched in inorganic content (*e.g.*, NaF, Na_2CO_3, Na_2O, and Na_3PO_4), facilitating Na^+ transport through the SEI layer. The formation of the SEI is also influenced by external factors such as temperature. Thenuwara *et al.*[72] reported that the SEI grown at −40 °C exhibits a mosaic structure, with inorganic crystallites embedded within an amorphous matrix. Cryo-HRTEM revealed lattice spacings consistent with Na_2CO_3, Na_2O, and Na_2SO_4 crystallites. At 20 °C, the SEI layer displays a similar structure but with larger crystallite sizes, measuring 306 ± 43 nm^2 compared to 191 ± 24 nm^2 at −40 °C (Fig. 3d).

Cryo-EM has also garnered significant interest in studies on solid-state sodium (Na) metal batteries. For instance, cryo-TEM was employed to analyze the interfacial structure of a composite sodium anode (CSA) incorporating a 3D superionic Na_3P skeleton in contact with the $Na_{3.1}Zr_{1.95}Mg_{0.05}Si_2PO_{12}$ (NZMSP) solid-state electrolyte.[73] The cryo-TEM images revealed a well-distributed and interconnected Na_3P network embedded within the Na matrix, which contributes to enhanced ion transport and uniform Na deposition. High-resolution images (Fig. 3e) further confirmed the presence of Na_3P (110) crystal planes with a d-spacing of 0.247 nm. Transitioning from purely ISEs to composite solid-state electrolytes (CSEs), cryo-TEM imaging further reveals that the SEI formed on Na with defect-engineered CSEs exhibits a mosaic nanostructure,[74] comprising crystalline Na_2O, Na_2CO_3, and NaF embedded in an amorphous organic matrix (Fig. 3f). These SEIs are highly crystalline and mechanically robust, effectively mitigating interfacial degradation and sustaining prolonged cycling, in sharp contrast to the brittle, inhomogeneous SEIs derived from conventional SEs. To address the interfacial instability of sodium metal in quasi-solid-state batteries, Li *et al.* employed *in situ* polymerization of butyl acrylate to regulate the electric double layer (EDL) at the Na interface *via* dipole interactions.[75] Cryo-TEM analysis reveals that this strategy leads to dense Na deposits with large grain sizes and a robust SEI dominated by NaF and Na_2S, in sharp contrast to the dendritic morphology and Na_2CO_3/NaOH-rich SEI in liquid electrolytes (Fig. 3g). The stabilized SEI effectively suppresses Na/electrolyte side reactions and improves Na^+ transport kinetics in Na metal batteries.

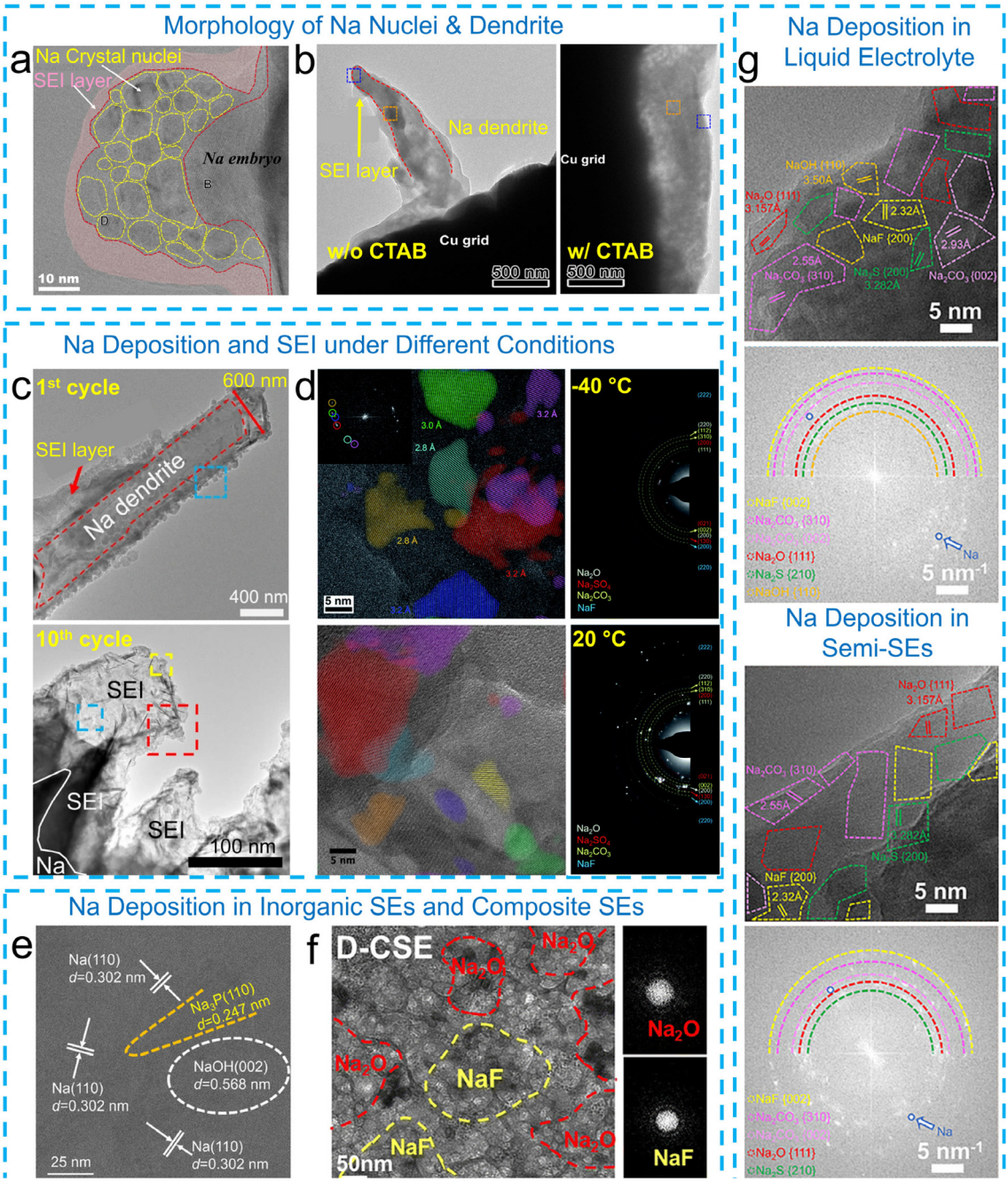

Fig. 3 Cryo-EM characterization of Na deposits and SEIs. (a) Na nuclei surrounding a Na embryo. Reproduced with permission from ref. 65. Copyright 2021 The Author(s). (b) Morphology of Na deposits formed in a $NaPF_6$-diglyme electrolyte with and without a CTAB additive. Reproduced with permission from ref. 66. Copyright 2022 American Chemical Society. (c) Morphology of Na deposits and the corresponding SEI layers formed in the 1st cycle and after the 10th cycle. Reproduced with permission from ref. 67. Copyright 2021 Springer Nature. (d) The composition of the SEI layer formed at −40 °C and 20 °C, respectively. Reproduced with permission from ref. 72. Copyright 2021 The Royal Society of Chemistry. (e) Cryo-TEM image of Na deposits in inorganic SEs ($Na_{3.1}Zr_{1.95}Mg_{0.05}Si_2PO_{12}$, NZMSP). Reproduced with permission from ref. 73. Copyright 2025 Wiley. (f) Cryo-TEM image of Na deposits in composite SEs (defect-rich carbon with poly(vinylidenefluoride-*co*-hexafluoropropylene) (PVDF-HFP)). Reproduced with permission from ref. 74. Copyright 2025 The Royal Society of Chemistry. (g) Cryo-TEM images and the corresponding FFT patterns of Na deposits formed in a liquid electrolyte (1 M NaFSI in PC with FEC) and a semi-solid electrolyte (poly(butyl acrylate) (PBA) added to 1 M NaFSI in PC with FEC). Reproduced with permission from ref. 75. Copyright 2025 Wiley.

3.2 Cryo-EM characterization of K metal interfaces and SEI features

The application of cryo-EM in K metal battery research remains in its early exploration stage, with only a few reports published to date.[76–79] Liu *et al.*[76] combined cryo-FIB/SEM and synchrotron X-ray nano-tomography (nano-XCT) to investigate the microstructure of K electrodeposits. Their study revealed that the wettability of the substrate critically influences K nucleation and growth, with a potassiophilic substrate, such as functionalized carbon cloth (FCC), promoting denser and more uniform K deposition compared to planar copper (Cu) foil (Fig. 4a). Moreover, the cryo-FIB technique revealed that engineered intermetallic (alkaline potassium–bismuth–telluride) supports within K metal anodes can effectively suppress filamentary deposition and promote dense, uniform metal growth.[80] The resulting SEI exhibits reduced porosity and enhanced structural integrity compared to conventional systems. Additionally, cryo-TEM characterization of electric double layer-regulated interfaces shows the formation of an inorganic-rich SEI with a stable morphology, which remains intact during extended cycling.[81] These findings underscore the critical role of interfacial structure in governing the electrochemical stability of K metal anodes.

Similar to Na, the interphase layer on K deposits is typically thicker and more complex due to the high reactivity of K metal.[82] Using low-dose (~8 e $Å^{-2}$ s^{-1} × 10 s) cryo-TEM combined with cryo-STEM-EDX and EELS, Zhang *et al.*[77] analyzed the composition and structure of the SEI on K deposits in a KFSI-TEP (triethyl phosphate) electrolyte. The SEI was found to be hundreds of nanometers thick and contained diverse, complex inorganic K salts, including KPO_3, K_2O, KO_2, K_2SO_4, and $K_2(SO_2)_3$, with a highly inhomogeneous distribution (Fig. 4b). Interestingly, interface engineering strategies can also lead to much thinner and more uniform SEI layers. For instance, cryo-TEM analysis of a high-entropy SEI formed on a Sn_9O_2/SnS_2 scaffold revealed a compact ~16 nm-thick SEI enriched with five distinct inorganic species (K_2SO_3, K_2CO_3,

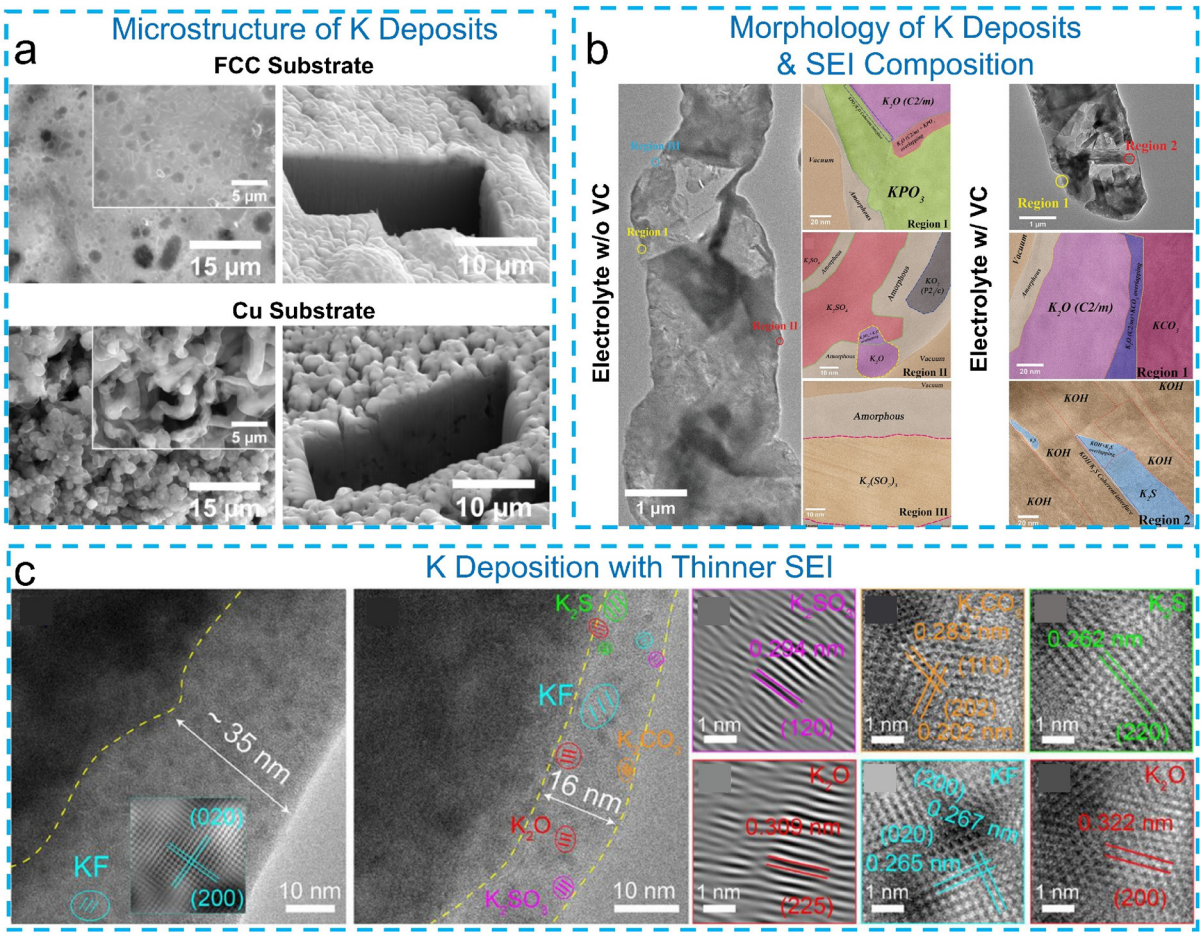

Fig. 4 (a) Cryo-FIB exposed the inner structure of K deposits formed on an FCC and Cu substrate, respectively. Reproduced with permission from ref. 76. Copyright 2023 Wiley. (b) Cryo-TEM images of the K deposits and SEIs formed in a KFSI-TEP and KFSI-TEP/2 wt% VC electrolyte, respectively. Reproduced with permission from ref. 77. Copyright 2021 Wiley. (c) Cryo-TEM images of K deposits on NF (3D nickel foam) and SnOS@NF, and the corresponding phase compositions of the high-entropy SEI on SnOS@NF with K metal deposition. Reproduced with permission from ref. 83. Copyright 2025 Wiley.

K_2S, K_2O, and KF),[83] as shown in Fig. 4c. This high-entropy SEI demonstrated improved ionic transport and mechanical robustness, underscoring the role of surface design in stabilizing K metal anodes.

Cryo-EM studies across Li, Na, and K systems reveal both shared interfacial principles and metal-specific behaviors. While all three alkali metals undergo surface-driven nucleation and form chemically heterogeneous SEI layers, their deposition morphologies and interphase structures differ markedly due to intrinsic physicochemical properties. Compared to Li, Na deposits typically exhibit larger grain sizes and thicker, more mosaic-like SEI layers, reflecting its lower reduction potential and higher surface mobility. In contrast, K metal, with its larger ionic radius and even higher chemical reactivity, tends to form substantially thicker and more compositionally complex interphases, often extending to hundreds of nanometers in conventional electrolytes. Cryo-EM further reveals that K-derived SEIs are generally more porous and structurally inhomogeneous unless interface engineering strategies are employed.

Moreover, the mechanical stability of the interphase appears to decrease from Li to Na to K, as evidenced by increased dendritic roughness, interfacial void formation, and structural fragmentation observed under cryogenic conditions. The systematic difference highlights that although alkali metals share similar electrochemical frameworks, their interfacial growth and degradation mechanisms cannot be directly extrapolated from Li to heavier counterparts. These observations further indicate that electrolyte composition and interphase chemistry must be tailored to the specific physicochemical properties of each metal system, underscoring the role of cryo-EM in guiding rational interface design for emerging metal batteries.

3.3 Cryo-EM characterization of multivalent metal anodes (Zn, Ca, and Mg)

The interfacial behavior of multivalent metal anodes remains far less understood compared to their monovalent counterparts such as Li, Na, and K. While Li metal typically forms a conformal solid–electrolyte interphase (SEI) that passivates the surface and regulates ion transport, multivalent metals like Zn, Ca, and Mg exhibit markedly different and more complex interfacial characteristics.

In particular, understanding and controlling the SEI on Zn metal is critical for improving reversibility and stability in aqueous and hybrid Zn batteries. Recent work by Guo *et al.*[84] demonstrated that a high-dipole-moment organophosphorus solvent, dimethyl methylphosphonate (DMMP), can induce an *in situ* monolithic phosphate SEI on Zn, significantly enhancing electrochemical performance. Notably, the FIB was applied to cut the Zn electrode into a lamella (Fig. 5a), which was then used for cryo-STEM analysis. Through cryo-STEM, a dense and uniform SEI (~300 nm) was observed (Fig. 5b), showing a chemically pure Zn–P–O composition. The lattice structure derived from the high-resolution mode further revealed a hybrid structure of crystalline $Zn_3(PO_4)_2$ and ZnP_2O_6 embedded in an amorphous matrix, offering strong adhesion and structural integrity. This integrated FIB and cryo-STEM workflow is insightful and worth adopting in related research.

In a recent study on Ca metal batteries, cryo-EM-based SAED and EELS mapping were employed to investigate the SEI structure on Ca deposits.[85] A nanoscale structure composed of heterogeneous oxides has been found for the SEI formed in a $Ca(BH_4)_2$-THF electrolyte. This SEI was sufficiently thin to enable Ca-ion diffusion while effectively protecting Ca metal from electrolyte corrosion, facilitating reversible Ca deposition. Additionally, Ca metal and CaH_2 were observed to coexist in Ca deposits, with CaH_2 enhancing Ca^{2+} transport and stabilizing Ca metal against self-discharge (Fig. 5c). Lu *et al.* used cryo-EM to investigate these interfaces in organoborate electrolytes for Ca and Mg metal batteries.[86] Mg deposited from the fully dissociated M2 electrolyte ($Mg(B(hfip)_4)_2$) formed large polygonal grains with visible (101) lattice fringes (Fig. 5d), while only sparse amorphous byproducts were observed, indicating the absence of a uniform SEI and suggesting that ion transport (not passivation) dominates its reversibility. Ca showed more complex behavior. In the fully dissociated C2 ($Ca(B(hfip)_4)_2$) and C3 ($Ca(BH(pftb)_3)_2$) electrolytes, Ca formed spherical deposits with amorphous passivation layers containing $CaCO_3$, CaF_2 nanocrystals, and amorphous CaH_x.

These results highlight cryo-EM's power in revealing subtle structural and compositional differences at the metal–electrolyte interface. Unlike the uniform SEI of Li, Zn, Mg, and Ca form heterogeneous and chemically reactive interphases, reflecting their unique electrochemical environments and underscoring the importance of solvation structure in interfacial engineering for multivalent batteries. Aqueous aluminum metal batteries (AAMBs) offer advantages such as low cost, high theoretical capacity, and intrinsic safety, but their practical application is limited by poor Al stability in aqueous electrolytes due to parasitic reactions like corrosion, passivation, and hydrogen evolution.[87,88] Although to the best of our knowledge, cryo-EM has not yet been applied to AAMB systems, its unique ability to visualize reactive and beam-sensitive interfaces with near-atomic resolution could provide critical insights into the formation and evolution of Al–electrolyte interphases, offering new opportunities to unravel degradation mechanisms and guide interface engineering in future AAMB research.

3.4 Understanding alloy metal anodes and interphase evolution *via* cryo-EM

Alloy-based metal anodes offer several advantages over pure alkali metal anodes, including improved mechanical stability, suppressed dendrite formation, and enhanced electrode–electrolyte interfacial contact, especially for solid electrolytes.[89,90] However, characterizing their SEIs remains challenging due to the complex phase distribution, chemical heterogeneity, and dynamic interfacial reactions. Cryo-EM provides a powerful tool to probe these interfaces with high spatial resolution while preserving their native structure, enabling new insights into the evolution of alloy-based interphases under realistic battery conditions.

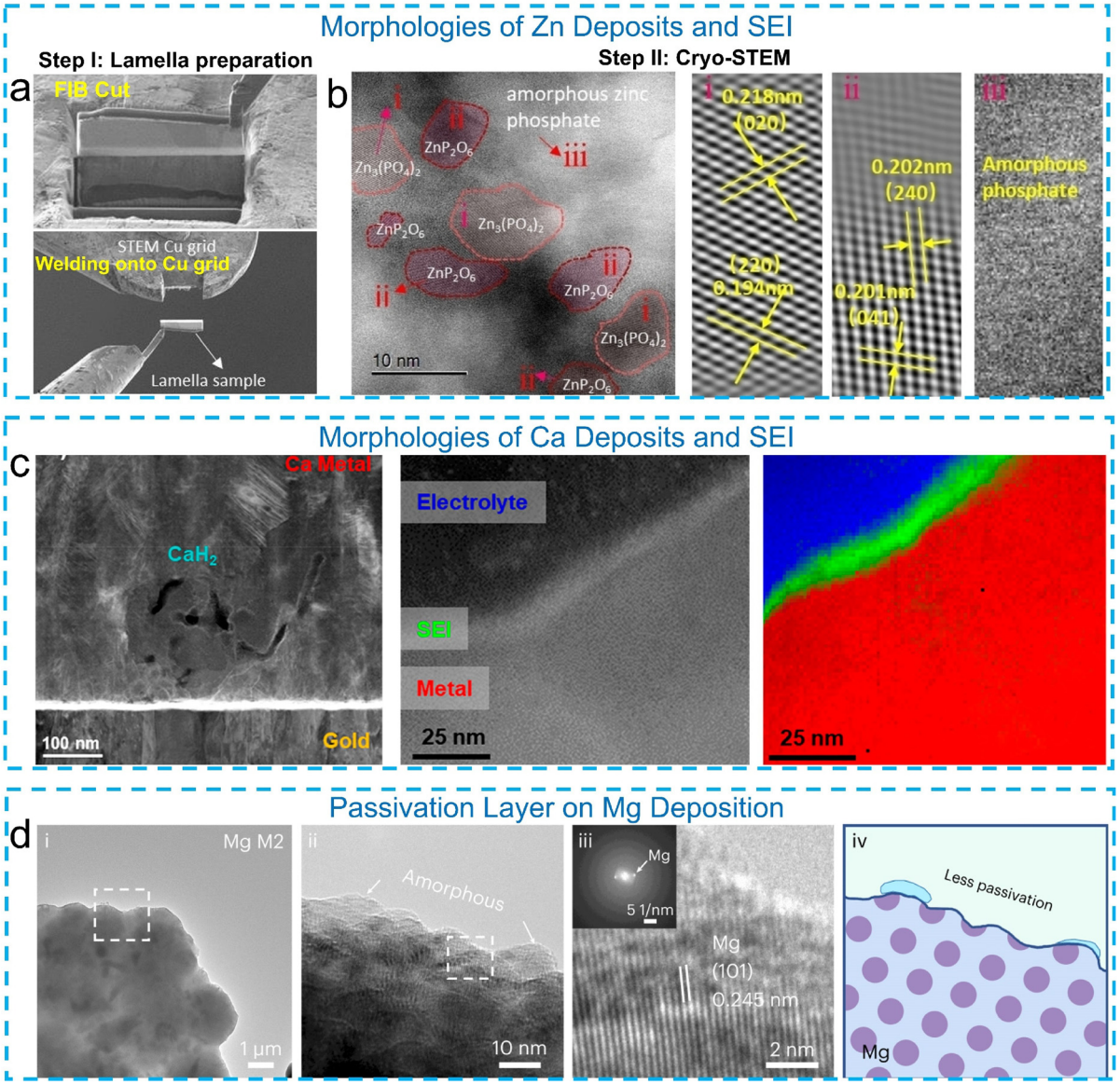

Fig. 5 (a) FIB preparation of a lamella sample from the Zn metal anode for cryo-STEM analysis. (b) Cryo-STEM image of the SEI structure in Zn metal batteries and the corresponding lattice structure. Reproduced with permission from ref. 84. Copyright 2023 Wiley. (c) Ca deposits and SEI composition revealed by cryo-STEM-EELS and SAED. Reproduced with permission from ref. 85. Copyright 2022 American Chemical Society. (d) Cryo-TEM image of the nanostructure of Mg deposits and SEIs formed in the M2 ($Mg(B(hfip)_4)_2$) electrolyte on the Mg metal anode. Reproduced with permission from ref. 86. Copyright 2024 The Author(s).

Cryo-TEM was employed to resolve the nanoscale structure of the lithiated InSnBi alloy anode in all-solid-state Li batteries, revealing uniformly dispersed In, Sn, and Bi elements, with abundant amorphous Li_xSn and Li_xIn phases surrounding nanosized crystalline Li_3Bi domains (Fig. 6a).[91] These amorphous phases effectively buffer volume fluctuations and relieve internal stress during cycling, preventing crack propagation within Li_2Bi. The resulting intact and well-distributed Li_3Bi network contributes to high ionic conductivity (>2 mS cm^{-1}) and robust electrochemical performance under high mass loading and low stack pressure conditions. Jeong *et al.* systematically investigated the electrochemical behavior of elemental alloy anodes in solid-state batteries with a Li_6PS_5Cl electrolyte, highlighting the critical influence of alloy composition on first-cycle CE.[92] Using cryo-FIB-SEM imaging, they revealed distinct lithiation and delithiation mechanisms across different metals. Indium showed exceptional CE (99.3%) due to its ability to retain the LiIn phase at the SSE interface during delithiation, enabling continuous Li transport and preventing trapping (Fig. 6b). In contrast, alloys such as Al, Sn, and Si formed pure elemental regions at the interface during delithiation, which led to lithium trapping and poor CE. Structural imaging confirmed that two-phase delithiation dynamics, volume changes, and transport limitations contrib-

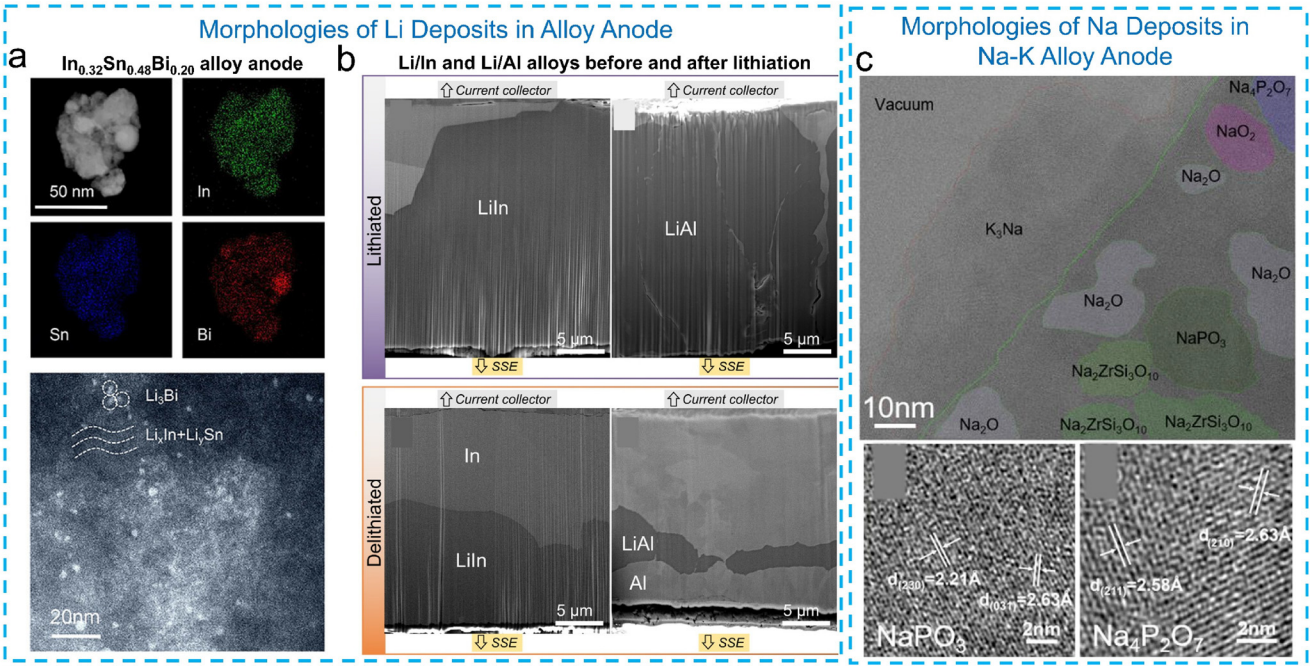

Fig. 6 (a) Cryo-TEM image of Li deposits in a lithiated InSnBi alloy anode and the corresponding EDX elemental mapping. Reproduced with permission from ref. 91. Copyright 2025 Wiley. (b) Cryo-FIB-SEM images of dense alloy anodes (Li–In and Li–Al) after lithiation and delithiation. Reproduced with permission from ref. 92. Copyright 2024 American Chemical Society. (c) Cryo-TEM image of Na deposits in the Na–K alloy anode and the corresponding selected areas for various inorganic components. Reproduced with permission from ref. 93. Copyright 2022 American Chemical Society.

ute to Li retention within the alloy matrix. The authors proposed that both lithium diffusion coefficients and the morphology of phase boundaries (*e.g.*, continuous *vs.* isolated regions) govern reversibility.

Gu *et al.*[93] conducted the first cryo-TEM study on Na–K alloy anodes in solid-state sodium metal batteries, revealing the detailed structure of the SEI after cycling. Cryo-HRTEM and FFT analyses (Fig. 6c) identified crystalline domains of Na oxides (Na_2O and NaO_2), Na phosphates ($Na_4P_2O_7$, $NaPO_3$), and $Na_2ZrSi_3O_{10}$, derived from interfacial redox reactions with the NaSICON-type solid electrolyte. Notably, the stable Na_2O phase localizes at the outer SEI, limiting further side reactions, while Na phosphates are distributed within an amorphous matrix, contributing to ionic conductivity. These findings suggest that the SEI formed from Na–K alloy exhibits a heterogeneous, mosaic-like structure, with both crystalline and disordered phases. Importantly, this SEI suppresses dendrite growth and enhances cycling longevity and critical current density (CCD), demonstrating the dual role of alloying and interphase engineering in stabilizing solid-state Na batteries.

Cryo-EM observations of alloy-based metal anodes further provide useful insights into the role of alloy phases in regulating metal nucleation and interfacial evolution. The direct visualization of alloy–metal interfaces and deposition behavior suggests that rational alloy design can effectively modulate local nucleation kinetics, reduce interfacial instability, and promote more uniform metal growth. These findings highlight the potential of alloy engineering as a practical strategy to stabilize reactive metal anodes and guide the development of advanced host materials for next-generation metal batteries.

3.5 Interfacial studies of anode-free batteries enabled by cryo-EM techniques

In addition to metal-anode systems, cryo-EM has also proven valuable for characterizing interfacial evolution in anode-free batteries, where controlling the metal ion's deposition morphology is critical. To this end, cryo-TEM and *in situ* SIMS were used to explore SEI formation dynamics during voltage-controlled cycling by Chen *et al.*[94] Cryo-TEM revealed that the SEI on the Cu current collector (CC) evolves progressively, forming a 6 nm layer after initial discharge and growing to ~14 nm after full charge–discharge (Fig. 7a). The observed SEI corresponds to a dense, inorganic-rich inner layer, while the soft organic outer layer may be lost during sample preparation. These results highlight that SEI formation is highly voltage-dependent and dynamic, with the inner and outer layers likely forming simultaneously and continuing to evolve during cycling. McDowell *et al.*[95] employed cryo-FIB milling combined with SEM imaging to study Li deposition on bare and alloy-modified CC (Fig. 7b). The cryo-FIB at −145 °C preserved the native morphology of deposited Li, whereas the room-temperature FIB caused substantial damage and distortion. By examining samples after successive deposition cycles, the authors showed that bare Cu led to nonuniform and unstable Li growth, while Ag and Au interfacial layers promoted more uniform deposition. Cryo-FIB/SEM imaging revealed

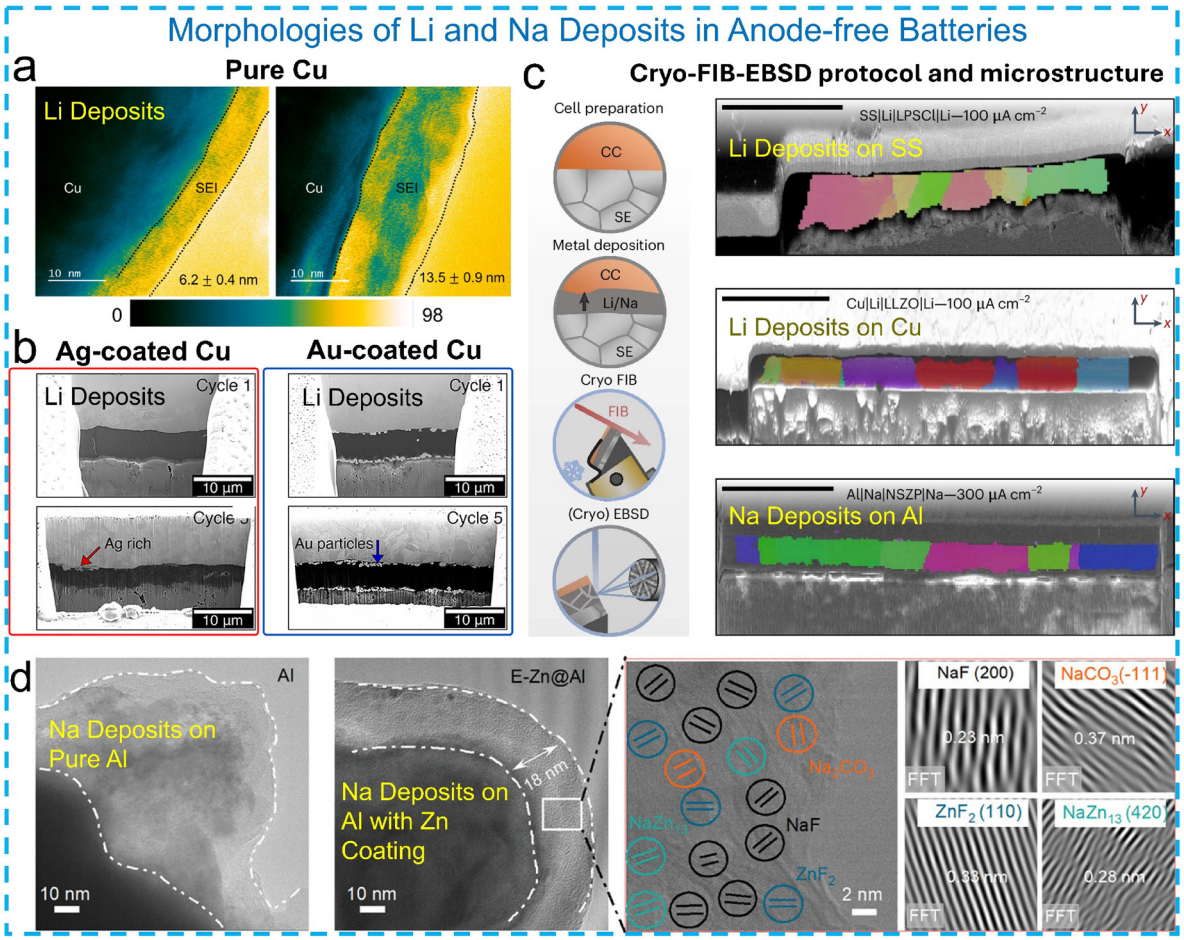

Fig. 7 (a) Cryo-TEM images of Li deposits on Cu CC and an SEI after charging to 3.0 V and discharging to 0.5 V, and an SEI after full charge–discharge (3.9–0.5 V). Reproduced with permission from ref. 94. Copyright 2023 American Chemical Society. (b) Cryo-FIB-SEM images of Li deposits onto bare Cu CC and Ag- and Au-modified Cu CC. Reproduced with permission from ref. 95. Copyright 2023 Elsevier. (c) Cryo-FIB and cryo-EBSD images of Li and Na deposits onto different CC|SE interfaces. Reproduced with permission from ref. 97. Copyright 2024 The Author(s). (d) Cryo-TEM of Na deposits onto Al and E-Zn@Al CC, and high-resolution cryo-TEM and FFT images of the lattice fringes in the SEI. Reproduced with permission from ref. 98. Copyright 2024 Wiley.

embedded Ag or Au structures and their morphological changes over cycling, such as Ag dissolution into Li and Au particle agglomeration, providing insight into their alloying behavior and impact on CEs.

Cryo-EM has also been applied to visualize the interphase structure in anode-free sodium metal batteries. Deysher *et al.*[96] employed cryo-FIB/SEM to expose and visualize the interfaces between Na deposits and an aluminum (Al) CC as well as the SEs. Fuchs *et al.*[97] established a protocol combining cryo-FIB sectioning with electron backscatter diffraction (EBSD) to investigate the microstructure of electrodeposited lithium and sodium metal films in anode-free solid-state batteries. Using cells with representative solid electrolytes (Li_6PS_5Cl, LLZO, and $Na_{3.4}Zr_2Si_{2.4}P_{0.6}O_{12}$), they observed large alkali metal (Li and Na) grain sizes ranging from 20 to 150 μm, significantly larger than typical electroplated metal films (Fig. 7c). The EBSD maps revealed well-defined grain orientations and grain boundary evolution, with Li and Na deposition showing preferential alignment and dynamic coarsening behavior. Notably, lithium plated at the Li_6PS_5Cl interface exhibited a short circuit but still allowed post-mortem structural analysis. This work demonstrates the value of EBSD in capturing mesoscopic grain evolution, complementing cryo-EM and SEM approaches by revealing a long-range texture and grain boundary morphology that influence current distribution and dendrite suppression in reservoir-free solid-state battery architectures.

Ge *et al.*[98] reported that in Na||Al cells, the Na metal becomes encapsulated by a thick, inhomogeneous SEI, leading to continuous sodium loss and poor cycling. In contrast, when using a flower-edged Zn-coated Al CC (E-Zn@Al), cryo-TEM revealed a uniform, ~18 nm-thick SEI with a well-defined boundary (Fig. 7d). High-resolution images and FFT analysis identified the SEI as composed of inorganic phases such as NaF, Na_2CO_3, ZnF_2, and $NaZn_{13}$. The presence of Zn-derived species was attributed to trace Zn^{2+} dissolution from the substrate, which reacts with PF6, a decomposition product. This

work highlights how cryo-TEM enables the nanostructural and compositional resolution of engineered SEIs in sodium systems and illustrates how substrate design and interfacial chemistry can synergistically enhance stability in anode-free configurations.

Cryo-EM studies of anode-free battery systems further provide important insights into the nucleation behavior of metal deposition on bare current collectors. Direct visualization of the early-stage nucleation process and interphase formation suggests that regulating the surface chemistry and interfacial structure of current collectors can effectively control metal nucleation and growth. These findings highlight the importance of interface engineering and electrolyte design in enabling uniform metal deposition and improving the cycling stability of anode-free metal batteries.

4. Summary of key insights from cryo-EM studies

As reviewed above, cryo-EM has proven to be a powerful tool for unveiling the nanostructure and crystallographic properties of Li and post-Li metal (Na, K, Zn, Ca, Mg, alloy, and anode-free) deposits, as well as the morphology, distribution, and partial chemical composition of their interphases. Specifically, cryo-EM has facilitated the detailed characterization of the morphology and crystallographic properties of Li deposits and provided insights into the thickness and structure of the SEI. These findings have supported the development of various models for Li nucleation (*e.g.*, SEI-induced nucleation) and growth (*e.g.*, tip and root growth), as well as SEI growth (*e.g.*, layered and mosaic structures).

In Li metal batteries, cryo-EM has enabled detailed characterization of Li deposition morphologies and crystallographic features, including dendritic growth directions, single-crystalline nanowire structures, and dynamic morphological evolution during cycling. These observations have contributed to the development of mechanistic models describing Li nucleation and growth, such as SEI-mediated nucleation and tip-growth and root-growth mechanisms, as well as structural models for SEI evolution, including layered and mosaic architectures. Beyond Li systems, cryo-EM studies have increasingly expanded to post-Li metal batteries. Early investigations on Na and K metal anodes have revealed distinct deposition behaviors and interphase structures that differ markedly from those of Li, reflecting differences in physicochemical properties such as ionic size, reduction potential, and interfacial reactivity. In multivalent systems such as Zn, Ca, and Mg, cryo-EM has begun to provide insights into deposition morphology, interfacial stability, and electrolyte–metal interactions. Furthermore, recent studies on alloy-based and anode-free configurations have highlighted how substrate composition, interfacial chemistry, and current collector surfaces influence metal nucleation and growth.

Despite these advances, the fundamental mechanisms governing metal nucleation, dendrite formation, and interphase evolution remain only partially understood, particularly during the early stages of deposition where transient interfacial processes occur. The strong dependence of these processes on electrolyte chemistry, interfacial structure, and electrochemical cycling conditions continues to pose challenges for direct characterization. Continuous development and broader application of cryo-EM techniques will therefore be essential for achieving a deeper mechanistic understanding of metal deposition and interphase evolution across diverse metal battery chemistries.

5. Challenges and prospects

5.1 Major challenges facing cryo-EM for the mechanistic study of reactive metal anodes and interphases

The application of cryo-EM to unravel the mechanisms of Li and post-Li metal deposition and interphase growth has reached a bottleneck. Specifically, the use of cryo-EM for battery characterization remains limited due to the scarcity of cryo-EM facilities within the materials science community and, more critically, the lack of a standardized workflow comparable to those established in structural biology. Currently, there is no universal cryo-EM workflow for sample preparation (*e.g.*, TEM lamella preparation), transfer (*e.g.*, using LN_2, vacuum, or inert gas), imaging (*e.g.*, an acceleration voltage of 200 or 300 kV and low-dose control), and image analysis (*e.g.*, accelerated processing and artifact correction during 3D reconstruction). The main technical challenges for establishing such an effective workflow are detailed as follows:

(i) In liquid electrolyte-based LMBs, cryo-EM sample preparation often involves placing TEM grids on a Cu current collector during cell assembly and depositing Li *in situ*. However, the influence of the TEM grid type and its selection criteria have not been systematically studied yet, remaining to be standardized.

(ii) The exact mechanisms and effects of electron beam damage on different metal deposits and interphases remain poorly understood, complicating the selection of optimal working conditions (*e.g.*, acceleration voltage, TEM *vs.* STEM mode). Zachman *et al.*[48] investigated electron beam-induced changes in cryogenic samples of Li deposits and SEIs under 300 kV conditions. They reported that the primary damage to metallic Li involves mass loss, accompanied by the formation of lithium oxides at doses exceeding 10^5 e^- $Å^{-2}$. Li salts such as Li_2O_2 and LiOH in the SEIs undergo mass loss at doses above 10^4 e^- $Å^{-2}$ and convert to Li_2O at higher doses, while Li_2O experiences only mass loss. Electrolyte components exhibit dose-dependent damage, with substantial mass loss occurring at 10^4 e^- $Å^{-2}$. However, the effects of electron beams on Li deposits under different working conditions (*e.g.*, 200 *vs.* 300 kV) and on post-Li metal deposits remain unexplored. Developing standardized protocols for low-dose control is essential but remains a challenge. Quantitative analysis based on EDX and EELS is particularly challenging due to the high susceptibility of samples to electron beam damage. These tech-

niques typically require high electron doses to produce sufficient signal, exacerbating damage to sensitive materials and making it difficult to accurately analyze amorphous components, such as amorphous Li and SEIs.

(iii) The development of a standardized cryo-EM workflow for SSBs and post-Li metal battery research presents additional challenges. High stacking pressure (*e.g.*, 10–50 MPa) is critical for the operation of SSBs. Under such conditions, ductile metal anodes adhere tightly to SEs, making it difficult to separate them for post-mortem analyses, particularly after long-term cycling, during which Li electrodes often become porous or even pulverized. These factors present significant obstacles to cryo-EM sample preparation to analyze interfaces/interphases between Li deposits and solid electrolytes. Reports have demonstrated the feasibility of preparing cryo-EM samples of Li deposits and SEIs from SPE-based SSBs using similar methods to those used for liquid electrolytes, as SPEs require relatively lower stacking pressures.[55,56] However, this approach is not viable for ISE-based SSBs, for which cryo-FIB remains the only reliable sample preparation method. Post-Li metal anodes, such as Na and K, pose even greater challenges due to their higher reactivity, which leads to strong surface reactions with residual H_2O, O_2, and N_2 during sample handling and transfer. These reactions compromise the accuracy of cryo-EM analysis, particularly for determining the chemical composition of interphases.

Next to the technical challenges related to the establishment of a standard workflow, the following major scientific questions remain unsolved.

(i) One critical challenge is to capture the form of Li nuclei. Despite cryo-EM's ability to mitigate electron beam damage, sub-/nanometer-sized Li nuclei remain elusive due to their extreme reactivity and sensitivity to electron beams. Electrochemical nucleation processes of heavier and air-stable metals are known to include multiple stages, *e.g.*, formation of atom seeds and/or sub-/nanometer clusters, which vary on the type of metal.[99] By contrast, Li deposits observed in the literature are typically larger than tens of nanometers, leaving the formation processes from Li seed atoms to sub-/nanometer atom clusters and eventually to nanocrystal nuclei unreported and hence poorly understood. This limitation hinders fundamental insights into Li nucleation and growth mechanisms.

(ii) A further challenge is visualizing interphases, particularly the "wet" SEI in liquid electrolytes. Historically, cryo-EM studies of SEIs have relied on "dry" SEI samples, which are extracted from batteries, washed with solvents, and dried before analysis. This approach is necessary due to the difficulty of directly imaging "wet" SEIs buried in frozen electrolytes under cryo-EM conditions. However, multiple changes may occur during sample preparation, including the dissolution of Li salts during washing. A recent study suggests that the SEI layer in liquid electrolytes exists in a swollen, gel-like state,[100] indicating that prior analyses of "dry" SEIs may not accurately represent their real and native properties in batteries.

5.2 Perspectives on the advancements of cryo-EM

While cryo-EM already incorporates an advanced set of techniques, further progress is needed to expand its application to sensitive energy materials. Enhancing its capabilities for studying the structure and dynamics of metal anodes and interphases is essential for gaining deeper mechanistic insights. These advancements will support the rational design of electrodes and batteries, driving the development of energy-dense and safe metal batteries for sustainable energy storage.

5.2.1 Standardization of a cryo-EM workflow for materials science. A standardized workflow for cryo-EM sample preparation, imaging, and data analysis has been successfully established in the field of structural biology. This workflow enables automated and high-throughput sample preparation, including cryo-FIB milling, transfer, and imaging.[101,102] The transfer of this expertise from structural biology to materials science has the potential to facilitate the development of a standardized and efficient cryo-EM workflow for studying sensitive energy materials.

Building a cryo-EM workflow for analyzing sensitive Li and post-Li metal anodes and interphases should prioritize the following aspects. Special attention should be given to the distinct properties of Li and post-Li metal electrodes when selecting operating conditions.

(i) Sample preparation from SSBs, including cryo-FIB and lift-out procedures for lamella preparation.

(ii) Sample transfer procedures that ensure appropriate transfer using LN_2, inert gas, or vacuum environments to preserve sample integrity.

(iii) Optimization of working voltage (*e.g.*, 200 or 300 kV) and imaging settings with a particular focus on low-dose control across different imaging modes (*e.g.*, HR-TEM, SAED, STEM-EDX/EELS, and ET).

(iv) Improvement of image processing and cryo-FIB & cryo-ET tomography analysis methods for reducing artifacts, accelerating segmentation and reconstruction, and enhancing accuracy by correlating artifacts with electron dosage and beam damage.

5.2.2 Advancements of cryo-EM instrumentation. In addition to workflow standardization, advancements in cryo-EM instrumentation are essential. Firstly, the development of new and more advanced instrumentation is necessary to enable faster and more precise analysis while minimizing electron beam damage to specimens. TEM instruments with improved detectors and cameras are critical for achieving higher image quality with reduced beam-induced damage. The development of multi-specimen grid holders can accelerate the time-consuming sample preparation and transfer processes. Combined with automated mechanical systems for sample transfer, these advancements would greatly facilitate the establishment of a high-throughput workflow.

Secondly, advancements in vitrification technology, particularly when combined with cryo-FIB, will enable the analysis of larger or thicker electrodes and even entire batteries. *In situ* cryo-EM characterization could be achieved through ultra-fast

freezing of reactive Li and post-Li metal electrodes together with their electrolytes, without the need for washing. Freezing methods such as slush nitrogen or liquid ethane could be employed to preserve the native state of electrodes and interphases within batteries. To facilitate efficient vitrification and prevent damage to specimens, specific cell designs such as thinner cell cases and electrodes will be required.

In addition, advancements in cryo-FIB instrumentation are crucial for minimizing ion beam damage to specimens. Cryogenic plasma focus ion beam (cryo-PFIB) has recently been developed to mitigate the effects of heavy ion beams on sensitive materials and enable high-volume material removal, yielding promising results.[97] However, further validation and broader adoption of cryo-PFIB in the battery research field remain necessary.

5.2.3 Toward *operando* cryo-EM: capturing dynamic interfacial processes. Another promising frontier lies in the development of *operando* cryo-EM techniques for metal battery systems. Unlike static imaging, *operando* approaches aim to capture the dynamic evolution of metal–electrolyte interfaces during actual electrochemical cycling. This is particularly critical for multivalent and alkali metal batteries, where interfacial structures evolve rapidly with cycling, influencing the deposition morphology, SEI composition, and failure mechanisms. However, achieving true *operando* cryo-EM remains technically challenging due to the need for precise control of temperature, vacuum, and electrochemical conditions, while preserving the native state of reactive interfaces. Future progress will require innovative cell designs compatible with cryogenic workflows, real-time cryo-transfer systems, and time-resolved imaging capabilities. Overcoming these hurdles will enable unprecedented insights into the transient states of interfaces, bridging the gap between atomic-scale snapshots and dynamic battery processes.

5.2.4 Development of new and emerging cryogenic analytical techniques. The application of cryo-EM for analyzing sensitive Li and post-Li deposits and interphases can be advanced through the integration and complement of new and emerging cryogenic microscopy techniques. These include cryo-EM-based methods, such as micro-electron diffraction (microED) and related techniques,[103] including vibrational EELS (vibEELS),[104] atom probe tomography (APT),[105] and transmission X-ray microscopy (TXM).[106]

(i) Cryo-STEM-based vibrational EELS (vibEELS) using an 'aloof' electron beam positioned tens of nanometers away from the specimen enables virtually damage-free vibrational spectroscopy analysis, minimizing beam damage to sensitive Li-related samples.[107] However, the hardware requirements for cryo-vibEELS are in high demand, with only a handful of instruments worldwide capable of achieving the required energy resolution of a few meV. Additionally, interpreting the complex spectra remains extremely challenging.

(ii) Cryo-microED, on the other hand, offers the potential for localized and detailed analysis of single-crystalline particles

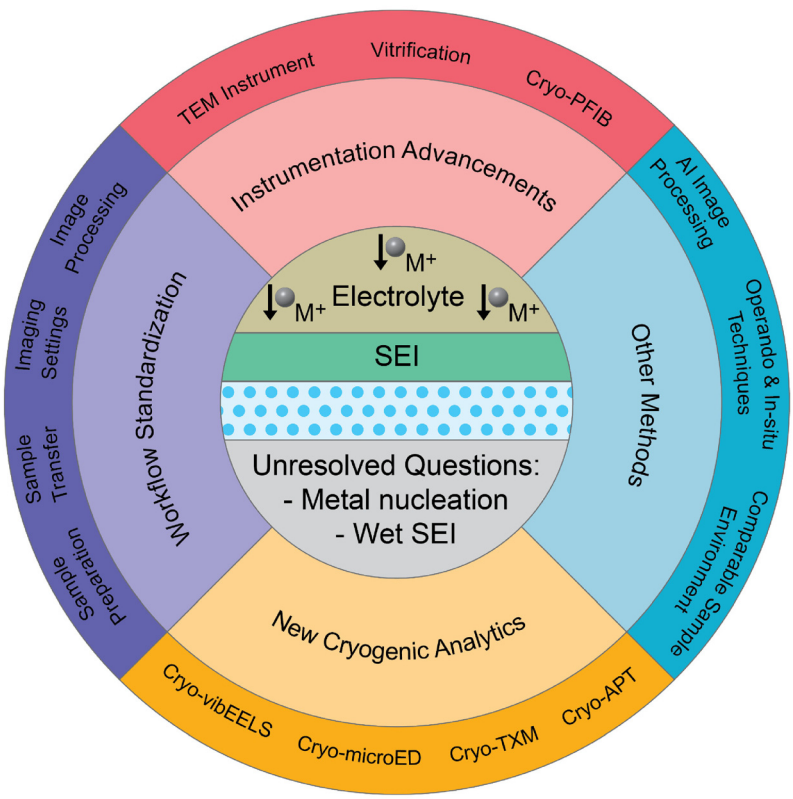

Fig. 8 Remaining challenges and future advancements of cryo-EM for investigating Li and post-Li metal electrodes and interphases.

within the specimen but is also expected to pose significant challenges. Consequently, substantial efforts are still required to integrate these techniques into a correlative cryo-EM workflow.

(iii) Cryo-TXM provides nanoscale morphological and chemical information with significantly lower radiation damage to specimens. However, its spatial resolution is limited to 10–50 nm, even when using a synchrotron X-ray source.

(iv) Cryo-APT protects sensitive specimens from ambient environmental exposure and enables detailed sub-nanometer-scale analysis of elemental distributions. It has demonstrated efficacy in characterizing $Li[Ni_xMn_yCo_{1-x-y}]O_2$ (NMC)[108] cathode and silicon (Si)[109] anode materials in the battery field. Nevertheless, accurately analyzing Li distribution in Li-containing samples remains extremely challenging due to the mobility and positional shifts of Li atoms, even under cryogenic conditions.

5.2.5 Correlation with other methods for an accurate and comprehensive understanding. The development of cryo-EM workflows, instrumentation, and new analytical techniques holds significant potential to open up new opportunities and break ground in the study of Li and post-Li metal deposits and interphases. However, realizing this potential requires a strong correlation of cryo-EM results with other characterization methods to achieve an accurate and comprehensive understanding.

Firstly, artificial intelligence (AI)-based virtual imaging offers the possibility of minimally invasive specimen analysis. Machine learning (ML)-based image processing and analysis can accelerate and improve the accuracy of cryo-EM data,[110] particularly for 3D segmentation and reconstruction. Additionally, developing high-throughput and random sampling methods combined with accelerated image processing is crucial for reliable analysis of large-area electrodes.

Moreover, it is essential to correlate non-*operando* and *ex situ* cryo-EM results with *operando* and *in situ* characterization techniques, such as *in situ* electrochemical TEM,[111] *operando* EC-AFM,[112] *in situ* XPS,[113] and *operando* FTIR.[114] These techniques provide complementary insights into the morphological and chemical evolution of Li and post-Li metal deposits and interphases in real-time during electrochemical cycling. A major challenge lies in achieving comparable operating conditions across different characterization methods, necessitating the development of common cell environments and integrated platforms for sample preparation and transfer. Correlation with electrochemical analytics, particularly charge transfer and ion transport kinetics, is also vital for understanding the electrochemical dynamics during battery operation.

Overall, cryo-EM has demonstrated success in the mechanistic studies of Li metal electrodes and interphases and has emerged as a valuable tool in post-Li metal battery research. Nevertheless, it faces substantial challenges in reaching its full potential (Fig. 8). Significant advancements in cryo-EM workflows, instrumentation, and data processing are urgently needed to achieve rapid, high-resolution, and accurate analysis of sensitive Li and post-Li metal deposits and interphases. These improvements will unlock new insights into metal anode electrochemistry and facilitate the rational design of high-performance electrodes and interfaces for advancing the development of next-generation battery systems.

Author contributions

Conceptualization: Y. Xu, Q. Wu, and Y. Lu; funding acquisition: Y. Lu; investigation: Y. Xu, K. Dong, and Z. Kochovski; methodology: Y. Xu, K. Dong, Z. Kochovski, Q. Wu, and Y. Lu; project administration: Y. Lu; resources: Y. Lu; supervision: Y. Lu; validation: Y. Xu and Q. Wu; visualization: Y. Xu, Z. Kochovski, and Q. Wu; writing – original draft: Y. Xu, K. Dong, Z. Kochovski, and Q. Wu; and writing – review & editing: Q. Wu and Y. Lu.

Conflicts of interest

There are no conflicts to declare.

Data availability

No primary research results, software or code have been included and no new data were generated or analysed as part of this perspective.

Acknowledgements

K. D. would like to acknowledge the National Natural Science Foundation of China (Grant No. 12405373) and the Science and Technology Innovation Program of the Institute of High Energy Physics, Chinese Academy of Sciences (No. E4545CU2 and E35451U2). Q. W. acknowledges Alexander von Humboldt's research fellowship.

References

1 Y. Tian, G. Zeng, A. Rutt, T. Shi, H. Kim, J. Wang, J. Koettgen, Y. Sun, B. Ouyang, T. Chen, Z. Lun, Z. Rong, K. Persson and G. Ceder, *Chem. Rev.*, 2021, **121**, 1623–1669, DOI: 10.1021/acs.chemrev.0c00767.
2 Y. Jie, C. Tang, Y. Xu, Y. Guo, W. Li, Y. Chen, H. Jia, J. Zhang, M. Yang, R. Cao, Y. Lu, J. Cho and S. Jiao, *Angew. Chem., Int. Ed.*, 2024, **63**, e202307802, DOI: 10.1002/anie.202307802.
3 J. Wang, B. Ge, H. Li, M. Yang, J. Wang, D. Liu, C. Fernandez, X. Chen and Q. Peng, *Chem. Eng. J.*, 2021, **420**, 129739, DOI: 10.1016/j.cej.2021.129739.
4 L. Yang, N. M. Hagh, J. Roy, E. Macciomei, J. R. Klein, U. Janakiraman and M. E. Fortier, *J. Electrochem. Soc.*, 2024, **171**, 060504, DOI: 10.1149/1945-7111/ad4ff2.
5 L. Qian, T. Or, Y. Zheng, M. Li, D. Karim, A. Cui, M. Ahmed, H. W. Park, Z. Zhang, Y. Deng, A. Yu, Z. Chen and K. Amine, *Renewables*, 2023, **1**, 114–141, DOI: 10.31635/renewables.023.202200014.

6 S. Wang, B. Peng, J. Lu, Y. Jie, X. Li, Y. Pan, Y. Han, R. Cao, D. Xu and S. Jiao, *Chem. – Eur. J.*, 2023, **29**, e202202380, DOI: 10.1002/chem.202202380.
7 J. Popovic, *J. Electrochem. Soc.*, 2022, **169**, 030510, DOI: 10.1149/1945-7111/ac580f.
8 X. Guo, S. Zhang, H. Hong, S. Wang, J. Zhu and C. Zhi, *iScience*, 2025, **28**, 111751, DOI: 10.1016/j.isci.2025.111751.
9 H. Song and C. Wang, *Adv. Energy Sustainability Res.*, 2022, **3**, 2100192, DOI: 10.1002/aesr.202100192.
10 C. You, X. Wu, X. Yuan, Y. Chen, L. Liu, Y. Zhu, L. Fu, Y. Wu, Y.-G. Guo and T. van Ree, *J. Mater. Chem. A*, 2020, **8**, 25601–25625, DOI: 10.1039/D0TA09330K.
11 X. Wang, S. Tang, W. Guo, Y. Fu and A. Manthiram, *Mater. Today*, 2021, **50**, 259–275, DOI: 10.1016/j.mattod.2021.05.001.
12 S. E. Sandoval, C. G. Haslam, B. S. Vishnugopi, D. W. Liao, J. S. Yoon, S. H. Park, Y. Wang, D. Mitlin, K. B. Hatzell, D. J. Siegel, P. P. Mukherjee, N. P. Dasgupta, J. Sakamoto and M. T. McDowell, *Nat. Mater.*, 2025, **24**, 673–681, DOI: 10.1038/s41563-024-02055-z.
13 Y. Xu, K. Dong, Y. Jie, P. Adelhelm, Y. Chen, L. Xu, P. Yu, J. Kim, Z. Kochovski, Z. Yu, W. Li, J. LeBeau, Y. Shao-Horn, R. Cao, S. Jiao, T. Cheng, I. Manke and Y. Lu, *Adv. Energy Mater.*, 2022, **12**, 2200398, DOI: 10.1002/aenm.202200398.
14 Q. Wu, Y. Mei, H. Huang, F. Zhou, H. Li and H. Chen, *Mater. Today*, 2024, **75**, 112–124, DOI: 10.1016/j.mattod.2024.04.011.
15 Z. Zeng, W. Zheng and H. Zheng, *Acc. Chem. Res.*, 2017, **50**, 1808–1817, DOI: 10.1021/acs.accounts.7b00161.
16 Z. Zeng, W.-I. Liang, H.-G. Liao, H. L. Xin, Y.-H. Chu and H. Zheng, *Nano Lett.*, 2014, **14**, 1745–1750, DOI: 10.1021/nl403922u.
17 H. Wang, *Sci. China:Life Sci.*, 2015, **58**, 750–756, DOI: 10.1007/s11427-015-4851-2.
18 J. Watt, D. L. Huber and P. L. Stewart, *MRS Bull.*, 2019, **44**, 942–948, DOI: 10.1557/mrs.2019.285.
19 Y. Li, W. Huang, Y. Li, W. Chiu and Y. Cui, *ACS Nano*, 2020, **14**, 9263–9276, DOI: 10.1021/acsnano.0c05020.
20 Y. Li, Y. Li, A. Pei, K. Yan, Y. Sun, C.-L. Wu, L.-M. Joubert, R. Chin, A. L. Koh, Y. Yu, J. Perrino, B. Butz, S. Chu and Y. Cui, *Science*, 2017, **358**, 506–510, DOI: 10.1126/science.aam6014.
21 D. Cheng, B. Lu, G. Raghavendran, M. Zhang and Y. S. Meng, *Matter*, 2022, **5**, 26–42, DOI: 10.1016/j.matt.2021.11.019.
22 X. Bai, Q. Huang, L. Wang, R. Yang, Z. Su and T. Jiang, *J. Alloys Compd.*, 2024, **1004**, 175913, DOI: 10.1016/j.jallcom.2024.175913.
23 S. Weng, Y. Li and X. Wang, *iScience*, 2021, **24**, 103402, DOI: 10.1016/j.isci.2021.103402.
24 X. Wang, Y. Li and Y. S. Meng, *Joule*, 2018, **2**, 2225–2234, DOI: 10.1016/j.joule.2018.10.005.
25 Y. Liu, Z. Ju, B. Zhang, Y. Wang, J. Nai, T. Liu and X. Tao, *Acc. Chem. Res.*, 2021, **54**, 2088–2099, DOI: 10.1021/acs.accounts.1c00120.
26 Z. Ju, H. Yuan, O. Sheng, T. Liu, J. Nai, Y. Wang, Y. Liu and X. Tao, *Small Sci.*, 2021, **1**, 2100055, DOI: 10.1002/smsc.202100055.
27 M. Yousaf, U. Naseer, A. Imran, Y. Li, W. Aftab, A. Mahmood, N. Mahmood, X. Zhang, P. Gao, Y. Lu, S. Guo, H. Pan and Y. Jiang, *Mater. Today*, 2022, **58**, 238–274, DOI: 10.1016/j.mattod.2022.06.022.
28 E. Zhang, M. Mecklenburg, X. Yuan, C. Wang, B. Liu and Y. Li, *iScience*, 2022, **25**, 105689, DOI: 10.1016/j.isci.2022.105689.
29 Y. Li, W. Zhou, Y. Li, W. Huang, Z. Zhang, G. Chen, H. Wang, G.-H. Wu, N. Rolston, R. Vila, W. Chiu and Y. Cui, *Joule*, 2019, **3**, 2854–2866, DOI: 10.1016/j.joule.2019.08.016.
30 Y. Zhu, Z. Gui, Q. Wang, F. Meng, S. Feng, B. Han, P. Wang, L. Huang, H.-L. Wang and M. Gu, *Nano Energy*, 2020, **73**, 104820, DOI: 10.1016/j.nanoen.2020.104820.
31 Y. Li, K. Wang, W. Zhou, Y. Li, R. Vila, W. Huang, H. Wang, G. Chen, G.-H. Wu, Y. Tsao, H. Wang, R. Sinclair, W. Chiu and Y. Cui, *Matter*, 2019, **1**, 428–438, DOI: 10.1016/j.matt.2019.06.001.
32 J. Li, C. Lin, T. Ma and J. Sun, *Nat. Commun.*, 2022, **13**, 4016, DOI: 10.1038/s41467-022-31524-9.
33 K. Liang, X. Yuan, X. Chen, B. Liu, J. T. Kim, J. Yu, D. Zhao and Y. Li, *Nano Lett.*, 2025, **25**, 7210–7223, DOI: 10.1021/acs.nanolett.5c00740.
34 M. Zhao, B.-Q. Li, X.-Q. Zhang, J.-Q. Huang and Q. Zhang, *ACS Cent. Sci.*, 2020, **6**, 1095–1104, DOI: 10.1021/acscentsci.0c00449.
35 Z. Liang, W. Wang and Y.-C. Lu, *Joule*, 2022, **6**, 2458–2473, DOI: 10.1016/j.joule.2022.10.008.
36 Z. Zhang and W.-Q. Han, *Nano-Micro Lett.*, 2023, **16**, 24, DOI: 10.1007/s40820-023-01234-y.
37 X.-B. Cheng, R. Zhang, C.-Z. Zhao and Q. Zhang, *Chem. Rev.*, 2017, **117**, 10403–10473, DOI: 10.1021/acs.chemrev.7b00115.
38 Q. Wu, Y. Zheng, X. Guan, J. Xu, F. Cao and C. Li, *Adv. Funct. Mater.*, 2021, **31**, 2101034, DOI: 10.1002/adfm.202101034.
39 H. Sun, Q. Liu, J. Chen, Y. Li, H. Ye, J. Zhao, L. Geng, Q. Dai, T. Yang, H. Li, Z. Wang, L. Zhang, Y. Tang and J. Huang, *ACS Nano*, 2021, **15**, 19070–19079, DOI: 10.1021/acsnano.1c04864.
40 X. Wang, G. Pawar, Y. Li, X. Ren, M. Zhang, B. Lu, A. Banerjee, P. Liu, E. J. Dufek, J.-G. Zhang, J. Xiao, J. Liu, Y. S. Meng and B. Liaw, *Nat. Mater.*, 2020, **19**, 1339–1345, DOI: 10.1038/s41563-020-0729-1.
41 K. Dong, Y. Xu, J. Tan, M. Osenberg, F. Sun, Z. Kochovski, D. T. Pham, S. Mei, A. Hilger, E. Ryan, Y. Lu, J. Banhart and I. Manke, *ACS Energy Lett.*, 2021, **6**, 1719–1728, DOI: 10.1021/acsenergylett.1c00551.
42 L. Zhang, T. Yang, C. Du, Q. Liu, Y. Tang, J. Zhao, B. Wang, T. Chen, Y. Sun, P. Jia, H. Li, L. Geng, J. Chen, H. Ye, Z. Wang, Y. Li, H. Sun, X. Li, Q. Dai, Y. Tang, Q. Peng, T. Shen, S. Zhang, T. Zhu and J. Huang, *Nat. Nanotechnol.*, 2020, **15**, 94–98, DOI: 10.1038/s41565-019-0604-x.
43 X. Yuan, B. Liu, M. Mecklenburg and Y. Li, *Nature*, 2023, **620**, 86–91, DOI: 10.1038/s41586-023-06235-w.

44 E. Peled, *J. Electrochem. Soc.*, 1979, **126**, 2047, DOI: 10.1149/1.2128859.
45 L. Wang, A. Menakath, F. Han, Y. Wang, P. Y. Zavalij, K. J. Gaskell, O. Borodin, D. Iuga, S. P. Brown, C. Wang, K. Xu and B. W. Eichhorn, *Nat. Chem.*, 2019, **11**, 789–796, DOI: 10.1038/s41557-019-0304-z.
46 J. Wang, W. Huang, A. Pei, Y. Li, F. Shi, X. Yu and Y. Cui, *Nat. Energy*, 2019, **4**, 664–670, DOI: 10.1038/s41560-019-0413-3.
47 Z. Shadike, H. Lee, O. Borodin, X. Cao, X. Fan, X. Wang, R. Lin, S.-M. Bak, S. Ghose, K. Xu, C. Wang, J. Liu, J. Xiao, X.-Q. Yang and E. Hu, *Nat. Nanotechnol.*, 2021, **16**, 549–554, DOI: 10.1038/s41565-020-00845-5.
48 M. J. Zachman, Z. Tu, S. Choudhury, L. A. Archer and L. F. Kourkoutis, *Nature*, 2018, **560**, 345–349, DOI: 10.1038/s41586-018-0397-3.
49 Y. Jie, Y. Xu, Y. Chen, M. Xie, Y. Liu, F. Huang, Z. Kochovski, Z. Lei, L. Zheng, P. Song, C. Hu, Z. Qi, X. Li, S. Wang, Y. Shen, L. Chen, Y. You, X. Ren, W. A. Goddard, R. Cao, Y. Lu, T. Cheng, K. Xu and S. Jiao, *Cell Rep. Phys. Sci.*, 2022, **3**, 101057, DOI: 10.1016/j.xcrp.2022.101057.
50 C. Wang, J. T. Kim, X. Yuan, J. K. Kim, B. Liu, M.-H. Kim, D. Zhao, M. Mecklenburg and Y. Li, *Sci. Adv.*, 2025, **11**, eadv3191, DOI: 10.1126/sciadv.adv3191.
51 J. Z. Lee, T. A. Wynn, M. A. Schroeder, J. Alvarado, X. Wang, K. Xu and Y. S. Meng, *ACS Energy Lett.*, 2019, **4**, 489–493, DOI: 10.1021/acsenergylett.8b02381.
52 B. Han, X. Li, S. Bai, Y. Zou, B. Lu, M. Zhang, X. Ma, Z. Chang, Y. S. Meng and M. Gu, *Matter*, 2021, **4**, 3741–3752, DOI: 10.1016/j.matt.2021.09.019.
53 M. Sun, T. Liu, Y. Yuan, M. Ling, N. Xu, Y. Liu, L. Yan, H. Li, C. Liu, Y. Lu, Y. Shi, Y. He, Y. Guo, X. Tao, C. Liang and J. Lu, *ACS Energy Lett.*, 2021, **6**, 451–458, DOI: 10.1021/acsenergylett.0c02314.
54 D. Cheng, T. A. Wynn, X. Wang, S. Wang, M. Zhang, R. Shimizu, S. Bai, H. Nguyen, C. Fang, M.-C. Kim, W. Li, B. Lu, S. J. Kim and Y. S. Meng, *Joule*, 2020, **4**, 2484–2500, DOI: 10.1016/j.joule.2020.08.013.
55 R. Lin, Y. He, C. Wang, P. Zou, E. Hu, X.-Q. Yang, K. Xu and H. L. Xin, *Nat. Nanotechnol.*, 2022, **17**, 768–776, DOI: 10.1038/s41565-022-01148-7.
56 K. Li, J. Wang, Q. Shen, Y. Song, R. Gao and Y. Wang, *Adv. Energy Mater.*, 2024, **14**, 2400956, DOI: 10.1002/aenm.202400956.
57 X. Lu, Y. Cheng, M. Li, Y. Zou, C. Zhen, D. Wu, X. Wei, X. Li, X. Yang and M. Gu, *Adv. Funct. Mater.*, 2023, **33**, 2212847, DOI: 10.1002/adfm.202212847.
58 V. Jabbari, V. Yurkiv, M. G. Rasul, A. H. Phakatkar, F. Mashayek and R. Shahbazian-Yassar, *Energy Storage Mater.*, 2023, **57**, 1–13, DOI: 10.1016/j.ensm.2023.02.009.
59 X. Zhang, Z. Guo, X. Li, Q. Liu, H. Hu, F. Li, Q. Huang, L. Zhang, Y. Tang and J. Huang, *Energy Environ. Sci.*, 2024, **17**, 1436–1447, DOI: 10.1039/D3EE04189A.
60 J. Lu, Y. Chen, Y. Lei, P. Jaumaux, H. Tian and G. Wang, *Nano-Micro Lett.*, 2025, **17**, 194, DOI: 10.1007/s40820-024-01632-w.
61 X. Zhang, M. Osenberg, R. F. Ziesche, Z. Yu, J. Kowal, K. Dong, Y. Lu and I. Manke, *ACS Energy Lett.*, 2025, **10**, 496–525, DOI: 10.1021/acsenergylett.4c02476.
62 Z. Zhao, G. Melinte, D. Guo, Y. Lei, M. N. Hedhili, X. Guo, Z. Shi, Y. Wang, J. K. El-Demellawi, W. Zhao and H. N. Alshareef, *Energy Environ. Sci.*, 2025, **18**, 2826–2838, DOI: 10.1039/D4EE05739B.
63 D. Petersen, M. Gronenberg, G. Lener, E. P. M. Leiva, G. L. Luque, S. Rostami, A. Paolella, B. J. Hwang, R. Adelung and M. Abdollahifar, *Mater. Horiz.*, 2024, **11**, 5914–5945, DOI: 10.1039/D4MH00529E.
64 X. Liu, X. Dong, H. Adenusi, Y. Wu and S. Passerini, *Nat. Rev. Chem.*, 2025, **9**, 415–426, DOI: 10.1038/s41570-025-00714-6.
65 Y. Zhu, Q. Zhang, X. Yang, M. Li, B. Wang and M. Gu, *iScience*, 2021, **24**, 103385, DOI: 10.1016/j.isci.2021.103385.
66 J. Luo, Y. Zhang, E. Matios, P. Wang, C. Wang, Y. Xu, X. Hu, H. Wang, B. Li and W. Li, *Nano Lett.*, 2022, **22**, 1382–1390, DOI: 10.1021/acs.nanolett.1c04835.
67 B. Han, Y. Zou, Z. Zhang, X. Yang, X. Shi, H. Meng, H. Wang, K. Xu, Y. Deng and M. Gu, *Nat. Commun.*, 2021, **12**, 3066, DOI: 10.1038/s41467-021-23368-6.
68 X. Zheng, S. Weng, W. Luo, B. Chen, X. Zhang, Z. Gu, H. Wang, X. Ye, X. Liu, L. Huang, X. Wu, X. Wang and Y. Huang, *Research*, 2022, **2022**, 9754612, DOI: 10.34133/2022/9754612.
69 B. Sayahpour, W. Li, S. Bai, B. Lu, B. Han, Y.-T. Chen, G. Deysher, S. Parab, P. Ridley, G. Raghavendran, L. H. B. Nguyen, M. Zhang and Y. S. Meng, *Energy Environ. Sci.*, 2024, **17**, 1216–1228, DOI: 10.1039/D3EE03141A.
70 K. C. Matthews, B. Rush, R. Gearba, X. Guo, G. Yu and J. H. Warner, *Adv. Mater.*, 2024, **36**, 2308711, DOI: 10.1002/adma.202308711.
71 N. Mubarak, F. Rehman, J. Wu, M. Ihsan-Ul-Haq, Y. Li, Y. Zhao, X. Shen, Z. Luo, B. Huang and J.-K. Kim, *Nano Energy*, 2021, **86**, 106132, DOI: 10.1016/j.nanoen.2021.106132.
72 A. C. Thenuwara, P. P. Shetty, N. Kondekar, C. Wang, W. Li and M. T. McDowell, *J. Mater. Chem. A*, 2021, **9**, 10992–11000, DOI: 10.1039/D1TA00842K.
73 C. Li, Y. Mu, T. Deng, Z. Li, G. Lu, R. Wang and C. Xu, *Adv. Mater.*, 2025, **37**, 2419190, DOI: 10.1002/adma.202419190.
74 L. Du, Y. Zhang, Y. Xiao, D. Yuan, M. Yao and Y. Zhang, *Energy Environ. Sci.*, 2025, **18**, 2949–2961, DOI: 10.1039/D4EE05966B.
75 Z. Li, J. Chen, Q. Fang, J. Fu, Y. Ren, X. Wang and X. Guo, *Angew. Chem., Int. Ed.*, 2025, **64**, e202505509, DOI: 10.1002/anie.202505509.
76 P. Liu, D. Yen, B. S. Vishnugopi, V. R. Kankanallu, D. Gürsoy, M. Ge, J. Watt, P. P. Mukherjee, Y.-C. K. Chen-Wiegart and D. Mitlin, *Angew. Chem., Int. Ed.*, 2023, **62**, e202300943, DOI: 10.1002/anie.202300943.
77 Q. Zhang, B. Han, Y. Zou, S. Shen, M. Li, X. Lu, M. Wang, Z. Guo, J. Yao, Z. Chang and M. Gu, *Adv. Mater.*, 2021, **33**, 2102666, DOI: 10.1002/adma.202102666.

78 X. Lian, Z. Ju, L. Li, Y. Yi, J. Zhou, Z. Chen, Y. Zhao, Z. Tian, Y. Su, Z. Xue, X. Chen, Y. Ding, X. Tao and J. Sun, *Adv. Mater.*, 2024, **36**, 2306992, DOI: 10.1002/adma.202306992.
79 P. Liu, H. Hao, A. Singla, B. S. Vishnugopi, J. Watt, P. P. Mukherjee and D. Mitlin, *Angew. Chem., Int. Ed.*, 2024, **63**, e202402214, DOI: 10.1002/anie.202402214.
80 R. Raj, Y. Wang, D. Yen, A. Singla, J. Diao, H. Hao, V. R. Kankanallu, B. S. Vishnugopi, M. Ge, J. Watt, G. Henkelman, Y.-C. K. Chen-Wiegart, P. P. Mukherjee and D. Mitlin, *Angew. Chem., Int. Ed.*, 2025, **64**, e202502213, DOI: 10.1002/anie.202502213.
81 X. Lian, L. Xu, Z. Ju, Z. Chen, X. Chen, Y. Yi, Z. Tian, T. Cheng, S. Dou, X. Tao and J. Sun, *Energy Environ. Sci.*, 2025, **18**, 322–333, DOI: 10.1039/D4EE03978E.
82 Y. Han, P. He and Y. Xu, *Joule*, 2025, **9**, 102053, DOI: 10.1016/j.joule.2025.102053.
83 L. Song, Q. Yang, Y. Yao, M. Tan, R. Li, J. Liao, X. Zhou and Y. Yu, *Angew. Chem., Int. Ed.*, 2025, **64**, e202509252, DOI: 10.1002/anie.202509252.
84 S. Liu, J. Vongsvivut, Y. Wang, R. Zhang, F. Yang, S. Zhang, K. Davey, J. Mao and Z. Guo, *Angew. Chem., Int. Ed.*, 2023, **62**, e202215600, DOI: 10.1002/anie.202215600.
85 S. A. McClary, D. M. Long, A. Sanz-Matias, P. G. Kotula, D. Prendergast, K. L. Jungjohann and K. R. Zavadil, *ACS Energy Lett.*, 2022, **7**, 2792–2800, DOI: 10.1021/acsenergylett.2c01443.
86 S. Li, J. Zhang, S. Zhang, Q. Liu, H. Cheng, L. Fan, W. Zhang, X. Wang, Q. Wu and Y. Lu, *Nat. Energy*, 2024, **9**, 285–297, DOI: 10.1038/s41560-023-01439-w.
87 H. Yu, X. Zhang, Y. Wang, M. Li, W. Chen, Z. Hu, M. Zhu and Y. Huang, *Adv. Mater.*, 2025, **37**, 2507164, DOI: 10.1002/adma.202507164.
88 M. Zhang, X. Tong, L. Zhu, F. Liu, Y. Jia, Z. Xiao, D. Fu, K. Han, Y. Wang, H. Zhang, X. Wang, J. Meng and Q. Pang, *Natl. Sci. Rev.*, 2025, **12**, nwaf233, DOI: 10.1093/nsr/nwaf233.
89 W. Jia, J. Zhang, L. Zheng, H. Zhou, W. Zou and L. Wang, *eScience*, 2024, **4**, 100266, DOI: 10.1016/j.esci.2024.100266.
90 J. Cao, Y. Shi, A. Gao, G. Du, M. Dilxat, Y. Zhang, M. Cai, G. Qian, X. Lu, F. Xie, Y. Sun and X. Lu, *Nat. Commun.*, 2024, **15**, 1354, DOI: 10.1038/s41467-024-45613-4.
91 Y. Sun, Y. Wu, Y. Yan, T. Liu, X. Du, D. Qu, T. Dong, L. Huang, A. Du, S. Zhang, S. Dong and G. Cui, *Adv. Mater.*, 2025, **37**, 2510128, DOI: 10.1002/adma.202510128.
92 W. J. Jeong, C. Wang, S. G. Yoon, Y. Liu, T. Chen and M. T. McDowell, *ACS Energy Lett.*, 2024, **9**, 2554–2563, DOI: 10.1021/acsenergylett.4c00915.
93 Y. Cheng, M. Li, X. Yang, X. Lu, D. Wu, Q. Zhang, Y. Zhu and M. Gu, *Nano Lett.*, 2022, **22**, 9614–9620, DOI: 10.1021/acs.nanolett.2c03718.
94 C. Cheng, Y. Zhou, Y. Xu, H. Jia, J. Kim, W. Xu, C. Wang, P. Gao and Z. Zhu, *Nano Lett.*, 2023, **23**, 8385–8391, DOI: 10.1021/acs.nanolett.3c00709.
95 S. E. Sandoval, J. A. Lewis, B. S. Vishnugopi, D. L. Nelson, M. M. Schneider, F. J. Q. Cortes, C. M. Matthews, J. Watt, M. Tian, P. Shevchenko, P. P. Mukherjee and M. T. McDowell, *Joule*, 2023, **7**, 2054–2073, DOI: 10.1016/j.joule.2023.07.022.
96 G. Deysher, J. A. S. Oh, Y.-T. Chen, B. Sayahpour, S.-Y. Ham, D. Cheng, P. Ridley, A. Cronk, S. W.-H. Lin, K. Qian, L. H. B. Nguyen, J. Jang and Y. S. Meng, *Nat. Energy*, 2024, **9**, 1161–1172, DOI: 10.1038/s41560-024-01569-9.
97 T. Fuchs, T. Ortmann, J. Becker, C. G. Haslam, M. Ziegler, V. K. Singh, M. Rohnke, B. Mogwitz, K. Peppler, L. F. Nazar, J. Sakamoto and J. Janek, *Nat. Mater.*, 2024, **23**, 1678–1685, DOI: 10.1038/s41563-024-02006-8.
98 J. Ge, C. Ma, Y. Zhang, P. Ma, J. Zhang, Z. Xie, L. Wen, G. Tang, Q. Wang, W. Li, X. Guo, Y. Guo, E. Zhang, Y. Zhang, L. Zhao and W. Chen, *Adv. Mater.*, 2025, **37**, 2413253, DOI: 10.1002/adma.202413253.
99 K. Cao, J. Biskupek, C. T. Stoppiello, R. L. McSweeney, T. W. Chamberlain, Z. Liu, K. Suenaga, S. T. Skowron, E. Besley, A. N. Khlobystov and U. Kaiser, *Nat. Chem.*, 2020, **12**, 921–928, DOI: 10.1038/s41557-020-0538-9.
100 Z. Zhang, Y. Li, R. Xu, W. Zhou, Y. Li, S. T. Oyakhire, Y. Wu, J. Xu, H. Wang, Z. Yu, D. T. Boyle, W. Huang, Y. Ye, H. Chen, J. Wan, Z. Bao, W. Chiu and Y. Cui, *Science*, 2022, **375**, 66–70, DOI: 10.1126/science.abi8703.
101 A. Cheng and Y. Yu, *Curr. Opin. Struct. Biol.*, 2024, **86**, 102795, DOI: 10.1016/j.sbi.2024.102795.
102 R. I. Koning, H. Vader, M. van Nugteren, P. A. Grocutt, W. Yang, L. L. R. Renault, A. J. Koster, A. C. F. Kamp and M. Schwertner, *Nat. Commun.*, 2022, **13**, 2985, DOI: 10.1038/s41467-022-30562-7.
103 B. L. Nannenga and T. Gonen, *Nat. Methods*, 2019, **16**, 369–379, DOI: 10.1038/s41592-019-0395-x.
104 O. L. Krivanek, T. C. Lovejoy, N. Dellby, T. Aoki, R. W. Carpenter, P. Rez, E. Soignard, J. Zhu, P. E. Batson, M. J. Lagos, R. F. Egerton and P. A. Crozier, *Nature*, 2014, **514**, 209–212, DOI: 10.1038/nature13870.
105 B. Gault, A. Chiaramonti, O. Cojocaru-Mirédin, P. Stender, R. Dubosq, C. Freysoldt, S. K. Makineni, T. Li, M. Moody and J. M. Cairney, *Nat. Rev. Methods Primers*, 2021, **1**, 51, DOI: 10.1038/s43586-021-00047-w.
106 G. Schneider, *Ultramicroscopy*, 1998, **75**, 85–104, DOI: 10.1016/S0304-3991(98)00054-0.
107 P. Rez, T. Aoki, K. March, D. Gur, O. L. Krivanek, N. Dellby, T. C. Lovejoy, S. G. Wolf and H. Cohen, *Nat. Commun.*, 2016, **7**, 10945, DOI: 10.1038/ncomms10945.
108 M. P. Singh, S.-H. Kim, X. Zhou, H. Kwak, A. Kwiatkowski da Silva, S. Antonov, L. S. Aota, C. Jung, Y. S. Jung and B. Gault, *Adv. Energy Sustainability Res.*, 2023, **4**, 2200121, DOI: 10.1002/aesr.202200121.
109 S.-H. Kim, K. Dong, H. Zhao, A. A. El-Zoka, X. Zhou, E. V. Woods, F. Giuliani, I. Manke, D. Raabe and B. Gault, *J. Phys. Chem. Lett.*, 2022, **13**, 8416–8421, DOI: 10.1021/acs.jpclett.2c02236.
110 A. Pratap and N. Sardana, *Mater. Today: Proc.*, 2022, **62**, 7341–7347, DOI: 10.1016/j.matpr.2022.01.200.
111 S. Dai, J. Zhang, J. Qu, X. Li, S. Cheng and C. Shan, *Renewables*, 2023, **1**, 57–72, DOI: 10.31635/renewables.022.202200006.

112 Z. Zhang, S. Said, K. Smith, R. Jervis, C. A. Howard, P. R. Shearing, D. J. L. Brett and T. S. Miller, *Adv. Energy Mater.*, 2021, **11**, 2101518, DOI: 10.1002/aenm.202101518.
113 S. Wi, V. Shutthanandan, B. M. Sivakumar, S. Thevuthasan, V. Prabhakaran, S. Roy, A. Karakoti and V. Murugesan, *J. Vac. Sci. Technol., A*, 2022, **40**, 010808, DOI: 10.1116/6.0001460.
114 M. M. Amaral, C. G. Real, V. Y. Yukuhiro, G. Doubek, P. S. Fernandez, G. Singh and H. Zanin, *J. Energy Chem.*, 2023, **81**, 472–491, DOI: 10.1016/j.jechem.2023.02.036.